RESEARCH ARTICLE

General closed-form inverse kinematics for arbitrary three-joint subproblems based on the product of exponential model

Tao SONG[a], Bo PAN (✉)[a], Guojun NIU[b], Jiawen YAN[a], Yili FU[a]

[a] *State Key Laboratory of Robotics and System, Harbin Institute of Technology, Harbin 150001, China*
[b] *School of Mechanical Engineering and Automation, Zhejiang Sci-Tech University, Hangzhou 310018, China*

✉ *Corresponding author. E-mail: mepanbo@hit.edu.cn (Bo PAN)*

ABSTRACT The inverse kinematics problems of robots are usually decomposed into several Paden–Kahan subproblems based on the product of exponential model. However, the simple combination of subproblems cannot solve all the inverse kinematics problems, and there is no common approach to solve arbitrary three-joint subproblems in an arbitrary postural relationship. The novel algebraic geometric (NAG) methods that obtain the general closed-form inverse kinematics for all types of three-joint subproblems are presented in this paper. The geometric and algebraic constraints are used as the conditions precedent to solve the inverse kinematics of three-joint subproblems. The NAG methods can be applied in the inverse kinematics of three-joint subproblems in an arbitrary postural relationship. The inverse kinematics simulations of all three-joint subproblems are implemented, and simulation results indicating that the inverse solutions are consistent with the given joint angles validate the general closed-form inverse kinematics. Huaque III minimally invasive surgical robot is used as the experimental platform for the simulation, and a master–slave tracking experiment is conducted to verify the NAG methods. The simulation result shows the inverse solutions and six sets given joint angles are consistent. Additionally, the mean and maximum of the master–slave tracking experiment for the closed-form solution are 0.1486 and 0.4777 mm, respectively, while the mean and maximum of the master–slave tracking experiment for the compensation method are 0.3188 and 0.6394 mm, respectively. The experiments results demonstrate that the closed-form solution is superior to the compensation method. The results verify the proposed general closed-form inverse kinematics based on the NAG methods.

KEYWORDS inverse kinematics, Paden–Kahan subproblems, three-joint subproblems, product of exponential, closed-form solution

1 Introduction

The inverse kinematics problem of a robot manipulator is one of the most fundamental steps to obtain the mapping relationship between the end-effector and the joint angles in real-time control and trajectory planning [1,2]. This problem has been widely studied in various fields, such as medical robotics [3–5], bionic robotics [6,7], reconfigurable robotics [8,9], and redundant manipulator [10]. There are multiple methods derived based on the Denavit–Harbenterg (D–H) model and the product of exponential (POE) model to solve the inverse kinematics problem. For the D–H model, the robot needs to satisfy the Pieper criterion that three adjacent joint axes intersect at a single point. When it does not meet the Pieper criterion, there are other methods that can be applied, such as iterative methods [11,12], genetic methods [13,14], and neural network [15,16]. Tang [5] adopted the two-step approximate and compensation solution method to solve the inverse solution of the surgical instrument that did not meet the Pieper criterion. The wrist length of the surgical instrument was ignored in the solution process, and the relative motion error of the surgical instrument was compensated. However, the relative motion error of the surgical instrument increased when instrument pose was close to the singularity. Xu et al. [12] presented the hierarchical iterative inverse kinematics algorithm, which consisted of two-level iterations.

The first-level iteration achieved accurate initial estimates through an extended heuristic iterative method. On this basis, the second-level iteration calculated all the joint angles. The proposed algorithm was applied to a six-degree-of-freedom (6-DOF) manipulator with a 2-DOF reduced wrist. Zhou et al. [14] took the motion constraints into account to design the fitness function and utilized the cosine adaptive genetic algorithm to complete the time-optimal trajectory planning. Tian and Xu [15] designed the convolutional neural network and the effective neural network visual layer pre-training method to control the robot arm end-to-end. The simulation result validated the efficiency of the proposed convolutional neural network. Although these methods can obtain the feasible inverse kinematics solution when the robot does not meet the Pieper criterion, they are time-consuming, and the completeness, convergence, and robustness of the inverse solution cannot be guaranteed. In addition, these methods based on the D–H model are complex to establish the local coordinate system between the adjacent joints, and plenty of specific analyses are required for each manipulator. Therefore, the requirement for the closed-form inverse solution is necessary because of its accuracy and real-time capability. If the trajectory of the end-effector is continuous, then the closed-form solutions of the joints are continuous. In theory, the closed-form solution based on the POE model is error-free, so the robot is not affected by the cumulative error.

The expression of joint axis in the POE model is different from that in the D–H model. In the POE model, the transform of an arbitrary rigid body with respect to the inertial coordinate system can be expressed by a screw displacement [17]. Hence, the singularity problem that happens when adjacent joints are parallel in the D–H model does not occur in the POE model [18,19]. Screw theory and POE formula are used to provide a simplified symbolic representation that can obtain definite geometric significance. Furthermore, the inverse kinematics solution based on the POE model is closed-form, which is the most desired form of the inverse solution. Paden–Kahan method [20] decomposed the integrated manipulator into three classes of subproblems that can be easily solved. However, the simple combination of subproblems cannot solve all inverse solutions. Chen and Gao [21] introduced 11 types of subproblems for different configurations, including revolute and prismatic joints, and presented the solutions of some subproblems. By contrast, the case where the axes of the first two joints do not intersect cannot be solved. Zhao et al. [22] expanded the three classes to 28 detailed types of subproblems, consequently enabling the inverse solution to be easily obtained by assembling several subproblems according to the configuration. The subproblem RRT (R: revolute, T: translational) case where two adjacent axes intersect was solved, but other complex cases were not mentioned. Tan et al. [23] extended the second subproblem by two axes,

and the exact solution was obtained. The extended case is where the rotation to a point at a fixed distance from a given point was solved in a constructed manipulator. Leoro et al. [24] presented a new subproblem where the adjacent joints are parallel and both perpendicular to the third axis, and the solving method was applied to the 6-DOF EverRobot RH12. Chen et al. [25] improved an existing subproblem where adjacent axes were parallel and applied to the 6-DOF Qianjiang-I robot. Li et al. [26] proposed a new subproblem where three adjacent axes intersect at one point, and a humanoid arm with the configuration of generalized SRU was taken as the paradigm to validate the correctness of the analytical formula. Wang et al. [27,28] proposed the general frame for arbitrary 3R subproblems based on the POE model, and special cases such as perpendicular and parallel between multiple axes were taken into account. Simulation and experiment were likewise carried out to verify the availability of the proposed method. Wang et al. [29] presented a novel analytical inverse kinematics method for the 7-DOF space station remote manipulator system, and the simulation results showed improved calculation accuracy.

As discussed in the literature, the aforementioned methods focus on three revolute joint subproblems. However, the mixture of prismatic and revolute joints is frequently used in practical working environments, and there is no general approach to solve arbitrary three-joint subproblems in arbitrary posture. As a consequence, novel algebraic geometric (NAG) methods are presented to obtain the general closed-form inverse kinematics of all types of three-joint subproblems in this paper. The geometric and algebraic constraints are used as the conditions precedent to solve the inverse kinematics of three-joint subproblems. The NAG methods can solve inverse kinematics of three-joint subproblems in an arbitrary postural relationship.

The content of the paper is organized as follows. Section 2 introduces some fundamental properties of the POE formula and screw theory. The NAG methods for all types of three-joint subproblems in arbitrary postural relationship are described in detail in Section 3. In Section 4, the inverse kinematics simulations of all three-joint subproblems are implemented, and simulation and the master–slave tracking experiment based on the Huaque III minimally invasive surgical robot are carried out to verify the effectiveness of proposed NAG methods. The paper is concluded in the final section.

2　Preliminary knowledge

2.1　Mathematical description of the POE formula

The POE formula of the kinematics of a 3-DOF serial robot has the following form:

$$\tilde{q} = e^{\hat{\xi}_1\theta_1}e^{\hat{\xi}_2\theta_2}e^{\hat{\xi}_3\theta_3}\tilde{p}, \qquad (1)$$

where $\boldsymbol{\xi}_i$ $(i = 1, 2, 3)$ represents the twist coordinate of the ith joint axis, θ_i $(i = 1, 2, 3)$ represents the generalized angle of the ith joint, $\boldsymbol{\xi} = \begin{bmatrix} \boldsymbol{\omega} \\ \boldsymbol{r} \times \boldsymbol{\omega} \end{bmatrix}$ represents the revolute joint twist, $\boldsymbol{\xi} = \begin{bmatrix} \boldsymbol{0}_{3\times1} \\ \boldsymbol{v} \end{bmatrix}$ represents the prismatic joint twist, $\boldsymbol{\omega}$ represents the unit directional vector of the revolute joint axis, $\boldsymbol{r}$ is the position vector of the reference point r of the revolute joint axis, $\boldsymbol{v}$ represents the unit directional vector of the translational joint axis, $\hat{\boldsymbol{\xi}}_i$ $(i = 1, 2, 3)$ represents the instantaneous joint twist of the ith joint axis, and $\tilde{q}$ and $\tilde{p}$ represent the homogeneous coordinate of points q and p, respectively. In addition, $e^{\hat{\xi}_i\theta_i}$ represents the rigid motion. For the revolute and translational joints, $e^{\hat{\xi}\theta}$ is expressed respectively as

$$e^{\hat{\xi}\theta} =$$

$$\begin{cases} \begin{bmatrix} \boldsymbol{I}_{3\times3} & \boldsymbol{v}\theta \\ \boldsymbol{0}_{1\times3} & 1 \end{bmatrix}, & \boldsymbol{\omega} = \boldsymbol{0}, \\ \begin{bmatrix} e^{\hat{\omega}\theta} & (\boldsymbol{I}_{3\times3} - e^{\hat{\omega}\theta})(\boldsymbol{\omega}\times(\boldsymbol{r}\times\boldsymbol{\omega})) + \theta\boldsymbol{\omega}\boldsymbol{\omega}^{\mathrm{T}}(\boldsymbol{r}\times\boldsymbol{\omega}) \\ \boldsymbol{0}_{1\times3} & 1 \end{bmatrix}, & \boldsymbol{\omega} \neq \boldsymbol{0}, \end{cases} \qquad (2)$$

where $\hat{\boldsymbol{\omega}}$ represents the skew-symmetric matrices of $\boldsymbol{\omega}$. $e^{\hat{\omega}\theta}$ is a rotation matrix and is equivalent to the rotation matrix $\boldsymbol{R} \in SO(3)$ according to Euler's theorem. $e^{\hat{\omega}\theta}$ can be expressed via Rodrigues' formula as

$$e^{\hat{\omega}\theta} = \boldsymbol{I} + \hat{\boldsymbol{\omega}}\sin\theta + \hat{\boldsymbol{\omega}}^2(1 - \cos\theta). \qquad (3)$$

2.2 Mathematical description of the POE formula

The Paden–Kahan subproblem 1 is $\tilde{q} = e^{\hat{\xi}\theta}\tilde{p}$ and can be transformed as

$$q = e^{\hat{\omega}\theta}(p - r) + r, \qquad (4)$$

where $\boldsymbol{q}$ and $\boldsymbol{p}$ represent the position vectors of points q and p, respectively. Substituting Rodrigues' formula for $e^{\hat{\omega}\theta}$ into the above equation yields

$$\boldsymbol{x}\sin\theta + \boldsymbol{y}\cos\theta + \boldsymbol{z} = \boldsymbol{0}, \qquad (5)$$

where $\boldsymbol{x} = \hat{\boldsymbol{\omega}}(\boldsymbol{p} - \boldsymbol{r}) \in R^{3\times1}$, $\boldsymbol{y} = -\hat{\boldsymbol{\omega}}^2(\boldsymbol{p} - \boldsymbol{r}) \in R^{3\times1}$, and $\boldsymbol{z} = \hat{\boldsymbol{\omega}}^2(\boldsymbol{p} - \boldsymbol{r}) + \boldsymbol{p} - \boldsymbol{q} \in R^{3\times1}$. Since $\boldsymbol{x}^{\mathrm{T}}\boldsymbol{y} = 0$ and $\boldsymbol{x}^{\mathrm{T}}\boldsymbol{x} = \boldsymbol{y}^{\mathrm{T}}\boldsymbol{y}$, θ can be solved by $\sin\theta = -\dfrac{\boldsymbol{x}^{\mathrm{T}}\boldsymbol{z}}{\boldsymbol{x}^{\mathrm{T}}\boldsymbol{x}}$ and $\cos\theta = -\dfrac{\boldsymbol{y}^{\mathrm{T}}\boldsymbol{z}}{\boldsymbol{y}^{\mathrm{T}}\boldsymbol{y}}$, respectively.

The distance preservation principle is applied to the solution of subproblems with a revolute joint, which is often accompanied by squaring both sides of the equation. For instance, there is a distance δ between two vectors $\boldsymbol{s}$ and $\boldsymbol{t}$ as $\delta = \|\boldsymbol{s} - \boldsymbol{t}\|$. Squaring both sides yields $\|\boldsymbol{s}\|^2 + \|\boldsymbol{t}\|^2 + 2\boldsymbol{t}^{\mathrm{T}}\boldsymbol{s} = \delta^2$.

3 NAG method for arbitrary three-joint subproblems

Three-joint subproblems are extensions of several base subproblems, with R for revolute joint and T for translational joint. In total, there are many types of three-joint subproblems, namely, RRR, RRT, RTR, TRR, RTT, TRT, TTR, and TTT. Equation (1) is transformed as follows

$$\tilde{p} = e^{-\hat{\xi}_3\theta_3}e^{-\hat{\xi}_2\theta_2}e^{-\hat{\xi}_1\theta_1}\tilde{q}. \qquad (6)$$

Combining Eqs. (1) and (6) easily derives the equivalence of RRT and RTT to TRR and TTR [21]. Hence, the general closed-form solutions of RRR, RRT, RTR, TRR, TRT, and TTT types of three-joint subproblems are derived, and the special postures of those three-joint subproblems are discussed in this paper.

3.1 NAG method realization for the RRR subproblem

For the RRR three-joint subproblem, point p is rotated around $\boldsymbol{\xi}_3$, $\boldsymbol{\xi}_2$, and $\boldsymbol{\xi}_1$ respectively by θ_3, θ_2, and θ_1 to point q. Point p rotates around $\boldsymbol{\xi}_3$ at θ_3 to point c and point q rotates around $\boldsymbol{\xi}_1$ at $-\theta_1$ to point d, as shown in Fig. 1. The vectors $\boldsymbol{c}$, $\boldsymbol{d}$, $\boldsymbol{p}$, $\boldsymbol{p}_1$, $\boldsymbol{p}_2$, $\boldsymbol{p}_3$, and $\boldsymbol{q}$ represent the position vectors of points c, d, p, p_1, p_2, p_3, and q, respectively. The representations below are consistent with the definition here. This means that $\boldsymbol{c} = e^{\hat{\omega}_3\theta_3}(\boldsymbol{p} - \boldsymbol{p}_3) + \boldsymbol{p}_3$ and $\boldsymbol{d} = e^{-\hat{\omega}_1\theta_1}(\boldsymbol{q} - \boldsymbol{p}_1) + \boldsymbol{p}_1$, where points p_1 and p_3 are located on the $\boldsymbol{\xi}_1$ and $\boldsymbol{\xi}_3$, respectively. Clearly, points c and d are located on the circle C_2 normal to $\boldsymbol{\xi}_2$. The twist $\boldsymbol{\xi}_2$ passes through point p_2. According to the geometric and algebraic constraints, this is easily accessible as

$$\boldsymbol{\omega}_2^{\mathrm{T}}(\boldsymbol{c} - \boldsymbol{d}) = 0, \qquad (7)$$

$$\|\boldsymbol{c} - \boldsymbol{p}_2\| = \|\boldsymbol{d} - \boldsymbol{p}_2\|. \qquad (8)$$

By substituting the expressions for points c and d into Eqs. (7) and (8) and squaring both sides of Eq. (8), $e^{-\hat{\omega}_1\theta_1}$ and $e^{\hat{\omega}_3\theta_3}$ are replaced by their Rodrigues' formulas. The above two equations are transformed as follows:

$$x_1\sin\theta_1 + y_1\cos\theta_1 + x_2\sin\theta_3 + y_2\cos\theta_3 + z_1 = 0, \qquad (9)$$

$$x_3\sin\theta_1 + y_3\cos\theta_1 + x_4\sin\theta_3 + y_4\cos\theta_3 + z_2 = 0, \qquad (10)$$

where $x_1 = -\boldsymbol{\omega}_2^{\mathrm{T}}\hat{\boldsymbol{\omega}}_1(\boldsymbol{q} - \boldsymbol{p}_1)$, $y_1 = -\boldsymbol{\omega}_2^{\mathrm{T}}\hat{\boldsymbol{\omega}}_1^2(\boldsymbol{q} - \boldsymbol{p}_1)$, $x_2 = -\boldsymbol{\omega}_2^{\mathrm{T}}\hat{\boldsymbol{\omega}}_3(\boldsymbol{p} - \boldsymbol{p}_3)$, $y_2 = \boldsymbol{\omega}_2^{\mathrm{T}}\hat{\boldsymbol{\omega}}_3^2(\boldsymbol{p} - \boldsymbol{p}_3)$, $z_1 = \boldsymbol{\omega}_2^{\mathrm{T}}[\hat{\boldsymbol{\omega}}_1^2(\boldsymbol{q} - \boldsymbol{p}_1) - \hat{\boldsymbol{\omega}}_3^2(\boldsymbol{p} - \boldsymbol{p}_3) + \boldsymbol{q} - \boldsymbol{p}]$, $x_3 = -2(\boldsymbol{p}_1 - \boldsymbol{p}_2)^{\mathrm{T}}\hat{\boldsymbol{\omega}}_1(\boldsymbol{q} - \boldsymbol{p}_1)$, $y_3 = -2(\boldsymbol{p}_1 - \boldsymbol{p}_2)^{\mathrm{T}}\hat{\boldsymbol{\omega}}_1^2(\boldsymbol{q} - \boldsymbol{p}_1)$, $x_4 = -2(\boldsymbol{p}_3 - \boldsymbol{p}_2)^{\mathrm{T}}\hat{\boldsymbol{\omega}}_3(\boldsymbol{p} - \boldsymbol{p}_3)$, $y_4 = 2(\boldsymbol{p}_3 - \boldsymbol{p}_2)^{\mathrm{T}}\hat{\boldsymbol{\omega}}_3^2(\boldsymbol{p} - \boldsymbol{p}_3)$, and $z_2 = \|\boldsymbol{q} - \boldsymbol{p}_1\|^2 + \|\boldsymbol{p}_1 - \boldsymbol{p}_2\|^2 - \|\boldsymbol{p} - \boldsymbol{p}_3\|^2 - \|\boldsymbol{p}_3 - \boldsymbol{p}_2\|^2 + 2(\boldsymbol{p}_1 - \boldsymbol{p}_2)^{\mathrm{T}}(\boldsymbol{I} + \hat{\boldsymbol{\omega}}_1^2)(\boldsymbol{q} - \boldsymbol{p}_1) - 2(\boldsymbol{p}_3 - \boldsymbol{p}_2)^{\mathrm{T}} \cdot (\boldsymbol{I} + \hat{\boldsymbol{\omega}}_3^2)(\boldsymbol{p} - \boldsymbol{p}_3)$.

For the revolute joints, $\boldsymbol{\omega}_1^{\mathrm{T}}\hat{\boldsymbol{\omega}}_2 = \boldsymbol{\omega}_2^{\mathrm{T}}\hat{\boldsymbol{\omega}}_1 = \boldsymbol{0}_{1\times3}$ holds if $\boldsymbol{\xi}_1$ is parallel to $\boldsymbol{\xi}_2$. The RRR three-joint subproblems for special configurations are explained and illustrated
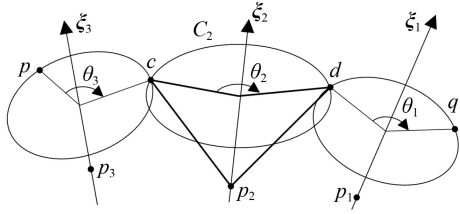
Fig. 1   General form of the RRR three-joint subproblem.

considering the property of parallel joint axes.

Category 1: $\boldsymbol{\xi}_2 \nparallel \boldsymbol{\xi}_1$ when $\boldsymbol{\xi}_2 \parallel \boldsymbol{\xi}_3$.

This category indicates $\boldsymbol{\omega}_2^{\mathrm{T}}\hat{\boldsymbol{\omega}}_3 = \mathbf{0}_{1\times3}$ and $\boldsymbol{\omega}_2^{\mathrm{T}}\hat{\boldsymbol{\omega}}_1 \neq \mathbf{0}_{1\times3}$. Then Eq. (9) is transformed to

$$x_1 \sin\theta_1 + y_1 \cos\theta_1 + z_1 = 0. \tag{11}$$

θ_1 can be solved by combining the above equation and the trigonometric relationship. If $x_1 \neq 0$, then $\theta_1 = \arcsin\dfrac{-z_1}{\sqrt{x_1^2+y_1^2}} - \arctan\dfrac{y_1}{x_1};$ if $y_1 \neq 0$, then $\theta_1 = \arccos\dfrac{-z_1}{\sqrt{x_1^2+y_1^2}} + \arctan\dfrac{x_1}{y_1}.$

The value of θ_1 is substituted into Eq. (10), and similarly, θ_3 can be solved. θ_2 can be solved by combining the value of θ_1, the value of θ_3, and Eq. (4).

Category 2: $\boldsymbol{\xi}_2 \nparallel \boldsymbol{\xi}_3$ when $\boldsymbol{\xi}_2 \parallel \boldsymbol{\xi}_1$.

This category indicates $\boldsymbol{\omega}_2^{\mathrm{T}}\hat{\boldsymbol{\omega}}_1 = \mathbf{0}_{1\times3}$ and $\boldsymbol{\omega}_2^{\mathrm{T}}\hat{\boldsymbol{\omega}}_3 \neq \mathbf{0}_{1\times3}$. Then Eq. (9) is transformed to

$$x_2 \sin\theta_3 + y_2 \cos\theta_3 + z_1 = 0. \tag{12}$$

Likewise, θ_3 can be solved by combining the above equation and the trigonometric relationship, and θ_1 can be solved by substituting the value of θ_3 into Eq. (10). θ_2 can be solved by combining the value of θ_1, the value of θ_3, and Eq. (4).

Category 3: $\boldsymbol{\xi}_2 \parallel \boldsymbol{\xi}_3$ when $\boldsymbol{\xi}_2 \parallel \boldsymbol{\xi}_1$.

This category indicates that $\boldsymbol{\omega}_2^{\mathrm{T}}\hat{\boldsymbol{\omega}}_1 = \mathbf{0}_{1\times3}$ and $\boldsymbol{\omega}_2^{\mathrm{T}}\hat{\boldsymbol{\omega}}_3 = \mathbf{0}_{1\times3}$. Points c, d, p_1, p_2, and p_3 are located on one plane. The plane passes through points p and q and is perpendicular to the twist $\boldsymbol{\xi}_2$. Therefore, the identity of Eq. (7) is always established. For Eq. (8), there are two cases here, namely, the unique solution or an infinite number of solutions. The case of the unique solution is shown in Fig. 2. Let $l_{12} = \|\boldsymbol{p}_1 - \boldsymbol{p}_2\|$, $l_{23} = \|\boldsymbol{p}_3 - \boldsymbol{p}_2\|$, $\delta_1 = \|\boldsymbol{q} - \boldsymbol{p}_1\|$, $\delta_3 = \|\boldsymbol{p} - \boldsymbol{p}_3\|$. l_{12} represents the distance between points p_1 and p_2, l_{23} represents the distance between points p_2 and p_3, δ_1 represents the distance between points q and p_1, and δ_3 represents the distance between points p and p_3. Assuming $l_{12} > l_{23}$, the following equation is satisfied when there is a unique solution; otherwise, there is an infinite number of solutions:

$$l_{12} - \delta_1 = l_{23} + \delta_3. \tag{13}$$

The locations of the transition points are $\boldsymbol{d} = \boldsymbol{p}_1 + (\boldsymbol{p}_2 - \boldsymbol{p}_1)\delta_1/l_{12}$ and $\boldsymbol{c} = \boldsymbol{p}_2 + (\boldsymbol{p}_3 - \boldsymbol{p}_2)(l_{23}+\delta_3)/l_{23}$. θ_1, θ_2, and θ_3 are solved by Eq. (4).

Conversely, if $l_{12} < l_{23}$, then $l_{12} + \delta_1 = l_{23} - \delta_3$ is satisfied when there is a unique solution.

Category 4: $\boldsymbol{\xi}_2 \nparallel \boldsymbol{\xi}_3$ when $\boldsymbol{\xi}_2 \nparallel \boldsymbol{\xi}_1$.

There are two cases in this category: Two adjacent axes are non-intersecting or two adjacent axes are intersected. For the case where two adjacent axes do not intersect, $x_1 y_3 - x_3 y_1 \neq 0$ and $x_2 y_4 - x_4 y_2 \neq 0$ hold at least one. Thus, Eqs. (9) and (10) can be written in the case of $x_1 y_3 - x_3 y_1 \neq 0$ as

$$\begin{cases} \sin\theta_1 = a_1 \sin\theta_3 + b_1 \cos\theta_3 + c_1, \\ \cos\theta_1 = a_2 \sin\theta_3 + b_2 \cos\theta_3 + c_2, \end{cases} \tag{14}$$

where $a_1 = \dfrac{x_4 y_1 - x_2 y_3}{x_1 y_3 - x_3 y_1}$, $b_1 = \dfrac{y_1 y_4 - y_2 y_3}{x_1 y_3 - x_3 y_1}$, $c_1 = \dfrac{y_1 z_2 - y_3 z_1}{x_1 y_3 - x_3 y_1}$, $a_2 = \dfrac{x_2 x_3 - x_1 x_4}{x_1 y_3 - x_3 y_1}$, $b_2 = \dfrac{x_3 y_2 - x_1 y_4}{x_1 y_3 - x_3 y_1}$, and $c_2 = \dfrac{x_3 z_1 - x_1 z_2}{x_3 z_1 - x_1 z_2}$.

Substituting Eq. (14) into $\sin^2\theta_1 + \cos^2\theta_1 = 1$ is written as

$$(a_1 \sin\theta_3 + b_1 \cos\theta_3 + c_1)^2 + (a_2 \sin\theta_3 + b_2 \cos\theta_3 + c_2)^2 = 1. \tag{15}$$

Let $t = \tan\theta_3/2$, then $\sin\theta_3 = 2t/(1+t^2)$ and $\cos\theta_3 = (1-t^2)/(1+t^2)$. These are substituted into Eq. (15) as

$$m_1 t^4 + m_2 t^3 + m_3 t^2 + m_4 t + m_5 = 0, \tag{16}$$

where $m_1 = (b_1 - c_1)^2 + (b_2 - c_2)^2 - 1$, $m_2 = 4[a_1(c_1 - b_1) + a_2(c_2 - b_2)]$, $m_3 = 2(2a_1^2 + 2a_2^2 - b_1^2 - b_2^2 + c_1^2 + c_2^2 - 1)$, $m_4 = 4[a_1(b_1 + c_1) + a_2(b_2 + c_2)]$, and $m_5 = (b_1 + c_1)^2 + (b_2 + c_2)^2 - 1$. For the quartic equation of Eq. (16), the solution of t is easily obtained by adopting Ferrari's method. The value of θ_3 can be solved as

$$\theta_3 = 2\arctan t. \tag{17}$$

The value of θ_3 is substituted into Eq. (14) to solve θ_1. Similarly, θ_2 can be solved by combining the value of θ_1, the value of θ_3, and Eq. (4).

The schematic for the case where two adjacent axes intersect is shown in Fig. 3. The twists $\boldsymbol{\xi}_1$ and $\boldsymbol{\xi}_2$ intersect at one point. Points c and d are located on one plane that
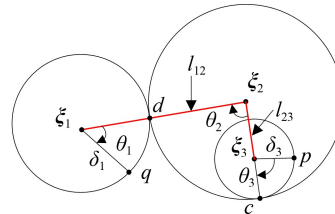

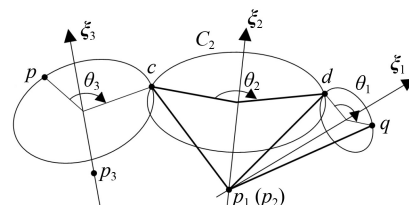**Fig. 2**   Form of the unique solution under triaxial parallelism.

Fig. 3   General form of the two adjacent axes of the RRR three-joint subproblem.

is perpendicular to the twist ξ_2. The geometric constraint is the same as Eq. (7), and algebraic constraint in Fig. 3 is

$$\|c - p_2\| = \|q - p_2\|. \tag{18}$$

By substituting the expression for point c into Eq. (18) and squaring both sides of Eq. (18), $e^{\hat{\omega}_3 \theta_3}$ is replaced by Rodrigues' formula. The above equation is transformed as follows:

$$a_1 \sin\theta_3 + b_1 \cos\theta_3 + c_1 = 0, \tag{19}$$

where $a_1 = 2(p_3 - p_2)^T \hat{\omega}_3 (p - p_3)$, $b_1 = -2(p_3 - p_2)^T \hat{\omega}_3^2 \cdot (p - p_3)$, and $c_1 = \|p - p_3\|^2 + \|p_3 - p_2\|^2 - \|q - p_2\|^2 + 2(p_3 - p_2)^T (I + \hat{\omega}_3^2)(p - p_3)$.

θ_3 can be solved by combining the above equation and the trigonometric relationship, and θ_1 can be solved by substituting the value of θ_3 into Eq. (9). θ_2 can be solved by combining the value of θ_1, the value of θ_3, and Eq. (4).

3.2 NAG method realization for the RRT subproblem

For the RRT three-joint subproblem, it is assumed that point p moves along ξ_3 by θ_3 to point c and point q rotates around ξ_1 at $-\theta_1$ to point d, as shown in Fig. 4. This means that $c = \theta_3 v_3 + p$ and $d = e^{-\hat{\omega}_1 \theta_1}(q - p_1) + p_1$, where p_1 is located on the ξ_1. It is obvious that points c and d are located on the circle C_2 normal to ξ_2. The twist ξ_2 passes through point p_2. This is easily accessible according to the geometric and algebraic constraints as

$$\omega_2^T(d - c) = 0, \tag{20}$$

$$\|c - p_2\| = \|d - p_2\|. \tag{21}$$

By substituting the expressions for points c and d into Eqs. (20) and (21), respectively, and squaring both sides of Eq. (21), $e^{-\hat{\omega}_1 \theta_1}$ is replaced by Rodrigues' formula. The above two equations are transformed as follows:

$$x_1 \sin\theta_1 + y_1 \cos\theta_1 + \lambda_1 \theta_3 + z_1 = 0, \tag{22}$$

$$x_2 \sin\theta_1 + y_2 \cos\theta_1 + \lambda_2 \theta_3^2 + \lambda_3 \theta_3 + z_2 = 0, \tag{23}$$

where $x_1 = -\omega_2^T \hat{\omega}_1 (q - p_1)$, $y_1 = -\omega_2^T \hat{\omega}_1^2 (q - p_1)$, $\lambda_1 = -\omega_2^T v_3$, $z_1 = \omega_2^T \left[\hat{\omega}_1^2 (q - p_1) + q - p \right]$, $x_2 = -2(p_1 - p_2)^T \hat{\omega}_1 \cdot (q - p_1)$, $y_2 = -2(p_1 - p_2)^T \hat{\omega}_1^2 (q - p_1)$, $\lambda_2 = -1$, $\lambda_3 =$

$-2(p - p_2)^T v_3$, $z_2 = \|q - p_1\|^2 + \|p_1 - p_2\|^2 - \|p - p_2\|^2 + 2(p_1 - p_2)^T (I + \hat{\omega}_1^2)(q - p_1)$.

For the revolute joints, $\omega_1^T \hat{\omega}_2 = \omega_2^T \hat{\omega}_1 = 0_{1\times3}$ holds if ξ_1 is parallel to ξ_2. For arbitrary two axes, $\omega_1^T \omega_2 = 0$ holds if ξ_1 is perpendicular to ξ_2. The RRT subproblems for special configurations are explained and illustrated considering the characteristics of parallel and vertical joint axes.

Category 1: $\xi_2 \parallel \xi_1$ when $\xi_2 \perp \xi_3$.

This category indicates $\omega_2^T \hat{\omega}_1 = 0_{1\times3}$ and $\omega_2^T v_3 = 0$. Points c, d, p_1, and p_2 are located on one plane. The plane passes through points p and q and is perpendicular to the twist ξ_2. Therefore, the identity of Eq. (20) is always established. For Eq. (23), there are two cases here: the unique solution or an infinite number of solutions, as shown in Figs. 5(a) and 5(b), respectively. Let $l_{12} = \|p_1 - p_2\|$, $l_{c2} = \|c - p_2\|$, and $\delta_1 = \|q - p_1\|$, where l_{12} represents the distance between the points p_1 and p_2, l_{c2} represents the distance between the points c and p_2, and δ_1 represents the distance between the points q and p_1. Point c is the tangent point between the circle C_2 and twist ξ_3, and $l_{12} + \delta_1 = l_{c2}$ is satisfied when there is a unique solution. This means that $c = p + v_3 v_3^T (p_2 - p)$. For the case of a unique solution, Eq. (23) should satisfy that θ_3 has a unique solution as follows:

$$\lambda_3^2 - 4\lambda_2 (x_2 \sin\theta_1 + y_2 \cos\theta_1 + z_2) = 0. \tag{24}$$

θ_1 can be solved by combining the above equation and the trigonometric relationship, and θ_3 can be solved by substituting the value of θ_1 into Eq. (23).

Another solution to this problem is to obtain $\theta_3 = -\lambda_3/(2\lambda_2)$ based on the fact that θ_3 has a unique solution. Then, θ_1 can be solved by substituting the value of θ_3 into Eq. (23) and the trigonometric relationship. θ_2
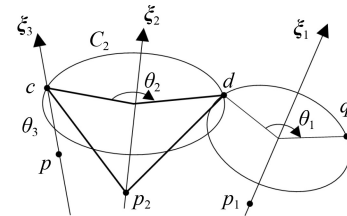

Fig. 4　General form of the RRT three-joint subproblem.
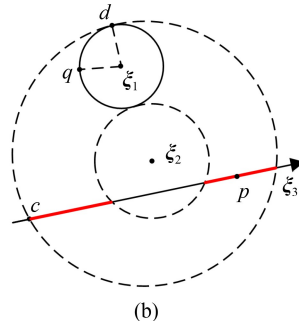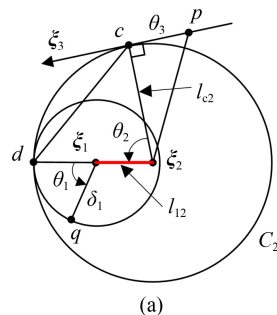

(a)

(b)

Fig. 5　Solution of RRT satisfying $\omega_2 \parallel \omega_1$ and $\omega_2 \perp v_3$. (a) Unique solution of category 1, (b) infinite number of solutions of category 1.

can be solved by combining the value of θ_1, the value of θ_3, and Eq. (4).

The infinite number of solutions of θ_3 are depicted as red line segments in Fig. 5(b), with the inverse solution of θ_3 at any point on the line segments.

Category 2: $\boldsymbol{\xi}_2$ is not parallel to $\boldsymbol{\xi}_1$ when $\boldsymbol{\xi}_2 \perp \boldsymbol{\xi}_3$.

This category indicates $\boldsymbol{\omega}_2^{\mathrm{T}}\hat{\boldsymbol{\omega}}_1 \neq \mathbf{0}_{1\times 3}$ and $\boldsymbol{\omega}_2^{\mathrm{T}}\boldsymbol{v}_3 = 0$. Then Eq. (22) is transformed to

$$x_1 \sin\theta_1 + y_1 \cos\theta_1 + z_1 = 0. \qquad (25)$$

θ_1 can be solved by combining the above equation and the trigonometric relationship. θ_3 can be solved by substituting the value of θ_1 into Eq. (23) and the trigonometric relationship. θ_2 can be solved by combining the value of θ_1, the value of θ_3, and Eq. (4).

Category 3: $\boldsymbol{\xi}_2 \parallel \boldsymbol{\xi}_1$ when $\boldsymbol{\xi}_2$ is not perpendicular to $\boldsymbol{\xi}_3$.

This category indicates $\boldsymbol{\omega}_2^{\mathrm{T}}\hat{\boldsymbol{\omega}}_1 = \mathbf{0}_{1\times 3}$ and $\boldsymbol{\omega}_2^{\mathrm{T}}\boldsymbol{v}_3 \neq 0$. Then θ_3 can be solved by $\theta_3 = -z_1/\lambda_1$ according to Eq. (22). The value of θ_3 is substituted into Eq. (23) to solve θ_1. θ_2 can be solved by combining the value of θ_1, the value of θ_3, and Eq. (4).

Category 4: $\boldsymbol{\xi}_2 \nparallel \boldsymbol{\xi}_1$ when $\boldsymbol{\xi}_2$ is not perpendicular to $\boldsymbol{\xi}_3$.

This category indicates $\boldsymbol{\omega}_2^{\mathrm{T}}\hat{\boldsymbol{\omega}}_1 \neq \mathbf{0}_{1\times 3}$ and $\boldsymbol{\omega}_2^{\mathrm{T}}\boldsymbol{v}_3 \neq 0$. If twists $\boldsymbol{\xi}_1$ and $\boldsymbol{\xi}_2$ intersect, the choices of points p_1 and p_2 should not be the point where the twists intersect. θ_3 is replaced with $\sin\theta_1$ and $\cos\theta_1$ in Eq. (22) and substituted into Eq. (23) as

$$a_1\sin^2\theta_1 + a_2\cos^2\theta_1 + a_3\sin\theta_1\cos\theta_1$$
$$+ a_4\sin\theta_1 + a_5\cos\theta_1 + a_6 = 0, \qquad (26)$$

where $a_1 = \lambda_2 x_1^2$, $a_2 = \lambda_2 y_1^2$, $a_3 = 2\lambda_2 x_1 y_1$, $a_4 = \lambda_1^2 x_2 + 2\lambda_2 x_1 z_1 - \lambda_1\lambda_3 x_1$, $a_5 = \lambda_1^2 y_2 + 2\lambda_2 y_1 z_1 - \lambda_1\lambda_3 y_1$, and $a_6 = \lambda_2 z_1^2 - \lambda_1\lambda_3 z_1 + \lambda_1^2 z_2$. Let $t = \tan\theta_1/2$, then $\theta_1 = \sin(2t)/(1+t^2)$ and $\cos\theta_1 = (1-t^2)/(1+t^2)$. Those are substituted into Eq. (26) as

$$m_1 t^4 + m_2 t^3 + m_3 t^2 + m_4 t + m_5 = 0, \qquad (27)$$

where $m_1 = a_2 - a_5 + a_6$, $m_2 = 2(a_4 - a_3)$, $m_3 = 2(2a_1 - a_2 + a_6)$, $m_4 = 2(a_3 + a_4)$, and $m_5 = a_2 + a_5 + a_6$. For the quartic equation of Eq. (27), the solution t is easily obtained by adopting Ferrari's method. The value of θ_1 can be solved as

$$\theta_1 = 2\arctan t. \qquad (28)$$

The value of θ_1 is substituted into Eq. (22) to solve θ_3. Similarly, θ_2 can be solved by combining the value of θ_1, the value of θ_3, and Eq. (4).

3.3 NAG method realization for the RTR subproblem

For the RTR three-joint subproblem, it is assumed that point p rotates around $\boldsymbol{\xi}_3$ at θ_3 to point c and point c moves along $\boldsymbol{\xi}_2$ by θ_2 to point d, as shown in Fig. 6. This means that $c = e^{\hat{\omega}_3\theta_3}(p - p_3) + p_3$ and $d = c + \theta_2 v_2$, where p_3 is located on the $\boldsymbol{\xi}_3$. Clearly, points d and q are located on the circle C_1 normal to $\boldsymbol{\xi}_1$. The twist $\boldsymbol{\xi}_1$ passes through
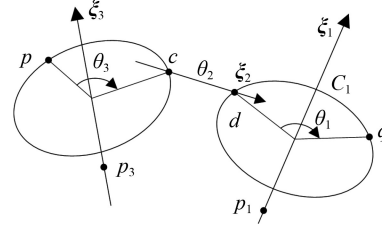

Fig. 6 General form of the RTR three-joint subproblem.

point p_1. This is easily accessible according to the geometric and algebraic constraints as

$$\boldsymbol{\omega}_1^{\mathrm{T}}(\boldsymbol{d} - \boldsymbol{q}) = 0, \qquad (29)$$

$$\|\boldsymbol{q} - \boldsymbol{p}_1\| = \|\boldsymbol{d} - \boldsymbol{p}_1\|. \qquad (30)$$

By substituting the expressions for points c and d into Eqs. (29) and (30), respectively, and squaring both sides of Eq. (30), $e^{\hat{\omega}_3\theta_3}$ is replaced by Rodrigues' formula. The above two equations are transformed as follows:

$$x_1\sin\theta_3 + y_1\cos\theta_3 + \lambda_1\theta_2 + z_1 = 0, \qquad (31)$$

$$x_2\sin\theta_3 + y_2\cos\theta_3 + \lambda_2\theta_2^2 + \lambda_3\theta_2$$
$$+ x_3\theta_2\sin\theta_3 + y_3\theta_2\cos\theta_3 + z_2 = 0, \qquad (32)$$

where $x_1 = \boldsymbol{\omega}_1^{\mathrm{T}}\hat{\boldsymbol{\omega}}_3(\boldsymbol{p} - \boldsymbol{p}_3)$, $y_1 = -\boldsymbol{\omega}_1^{\mathrm{T}}\hat{\boldsymbol{\omega}}_3^2(\boldsymbol{p} - \boldsymbol{p}_3)$, $\lambda_1 = \boldsymbol{\omega}_1^{\mathrm{T}}\boldsymbol{v}_2$, $z_1 = \boldsymbol{\omega}_1^{\mathrm{T}}\left(\hat{\boldsymbol{\omega}}_3^2(\boldsymbol{p} - \boldsymbol{p}_3) + \boldsymbol{p} - \boldsymbol{q}\right)$, $x_2 = 2(\boldsymbol{p}_3 - \boldsymbol{p}_1)^{\mathrm{T}}\hat{\boldsymbol{\omega}}_3(\boldsymbol{p} - \boldsymbol{p}_3)$, $y_2 = -2(\boldsymbol{p}_3 - \boldsymbol{p}_1)^{\mathrm{T}}\hat{\boldsymbol{\omega}}_3^2(\boldsymbol{p} - \boldsymbol{p}_3)$, $\lambda_2 = 1$, $\lambda_3 = 2\boldsymbol{v}_2^{\mathrm{T}}\left[(\boldsymbol{I} + \hat{\boldsymbol{\omega}}_3^2)(\boldsymbol{p} - \boldsymbol{p}_3) + (\boldsymbol{p}_3 - \boldsymbol{p}_1)\right]$, $x_3 = 2\boldsymbol{v}_2^{\mathrm{T}}\hat{\boldsymbol{\omega}}_3(\boldsymbol{p} - \boldsymbol{p}_3)$, $y_3 = -2\boldsymbol{v}_2^{\mathrm{T}}\hat{\boldsymbol{\omega}}_3^2(\boldsymbol{p} - \boldsymbol{p}_3)$, $z_2 = \|\boldsymbol{p} - \boldsymbol{p}_3\|^2 + \|\boldsymbol{p}_3 - \boldsymbol{p}_1\|^2 - \|\boldsymbol{q} - \boldsymbol{p}_1\|^2 + 2(\boldsymbol{p}_3 - \boldsymbol{p}_1)^{\mathrm{T}}(\boldsymbol{I} + \hat{\boldsymbol{\omega}}_3)(\boldsymbol{p} - \boldsymbol{p}_3)$.

For the revolute joints, $\boldsymbol{\omega}_1^{\mathrm{T}}\hat{\boldsymbol{\omega}}_2 = \boldsymbol{\omega}_2^{\mathrm{T}}\hat{\boldsymbol{\omega}}_1 = \mathbf{0}_{1\times 3}$ holds if $\boldsymbol{\xi}_1$ is parallel to $\boldsymbol{\xi}_2$. For two arbitrary axes, $\boldsymbol{\omega}_1^{\mathrm{T}}\boldsymbol{\omega}_2 = 0$ holds if $\boldsymbol{\xi}_1$ is perpendicular to $\boldsymbol{\xi}_2$. The RTR three-joint subproblems for special configurations are explained and illustrated considering the characteristics of parallel and vertical joint axes.

Category 1: $\boldsymbol{\xi}_1 \parallel \boldsymbol{\xi}_3$ when $\boldsymbol{\xi}_1 \perp \boldsymbol{\xi}_2$.

This category indicates $\boldsymbol{\omega}_3^{\mathrm{T}}\hat{\boldsymbol{\omega}}_1 = \mathbf{0}_{1\times 3}$ and $\boldsymbol{\omega}_1^{\mathrm{T}}\boldsymbol{v}_2 = 0$. Points c, d, p_1, and p_3 are located on one plane, which passes through points p and q and is perpendicular to the twist $\boldsymbol{\xi}_1$. Therefore, the identity of Eq. (29) is always established. For Eq. (32), there are two cases here, namely, the unique solution or an infinite number of solutions, as shown in Figs. 7(a) and 7(b), respectively. For the unique solution of special posture, both transition points c and d are tangent points, and both $\boldsymbol{\xi}_1$ and $\boldsymbol{\xi}_3$ are on opposite sides of $\boldsymbol{\xi}_2$, as shown in Fig. 7(a). Let $\delta_1 = \|\boldsymbol{p} - \boldsymbol{p}_3\|$, $\delta_3 = \|\boldsymbol{q} - \boldsymbol{p}_1\|$, and $\boldsymbol{p}_{13} = \boldsymbol{p}_1 - \boldsymbol{p}_3$, where δ_1 represents the distance between the points p and p_3, δ_3 represents the distance between the points q and p_1, and $\boldsymbol{p}_{13}$ represents the difference between the vectors $\boldsymbol{p}_1$ and $\boldsymbol{p}_3$. When $\|\boldsymbol{p}_{13} - \boldsymbol{v}_2\boldsymbol{v}_2^{\mathrm{T}}\boldsymbol{p}_{13}\| = \delta_1 + \delta_3$ is satisfied, it means that there is a unique solution; otherwise, there is an infinite number of solutions. The position solutions of the two tangent points c and d have the most critical selections. The solution for the position of point c is used as an example, as shown in Fig. 8.
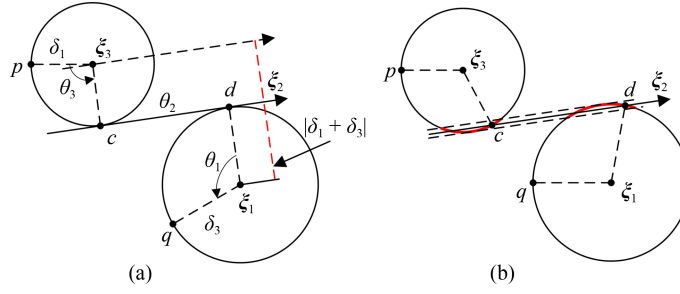
Fig. 7 Solution of RTR satisfying $\omega_1 \parallel \omega_3$ and $\omega_1 \perp v_2$. (a) Unique solution of category 1, (b) infinite number of solutions of category 1.
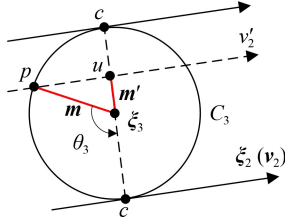
Fig. 8 Solution for the position of point c.

As seen from Fig. 8, point c is the tangent point of circle C_3 and twist ξ_2. Let $m = p_3 - p$, the vector m represents the difference between the vectors p_3 and p, and the projection of the vector m on ξ_2 is $v_2 v_2^T m$. Thus, $m' = m - v_2 v_2^T m$ can be obtained. Since the tangent point of a line and a circle may exist in two opposite directions, the location of point c is $c = p_3 \pm \|m\| \cdot \dfrac{m'}{\|m'\|}$. Similarly, the position of point d can be solved and then θ_2 can be solved from $\theta_2 = \|d - c\|/\|v_2\|$. The value of θ_2 is substituted into Eq. (32) to solve θ_3. θ_1 can be solved by combining the value of θ_2, the value of θ_3, and Eq. (4).

The infinite number of solutions of θ_3 is depicted as the red circular arc segments in Fig. 7(b), with the inverse solution of θ_3 at any point on the red circular arc segments.

Category 2: $\xi_1 \nparallel \xi_3$ when $\xi_1 \perp \xi_2$.

This category indicates $\omega_3^T \omega_1 \neq \mathbf{0}_{1 \times 3}$ and $\omega_1^T v_2 = 0$. Then Eq. (31) is transformed to

$$x_1 \sin\theta_3 + y_1 \cos\theta_3 + z_1 = 0. \tag{33}$$

θ_3 can be solved by combining the above equation and the trigonometric relationship. θ_2 can be solved by substituting the value of θ_3 into Eq. (32). θ_1 can be solved by combining the value of θ_2, the value of θ_3, and Eq. (4).

Category 3: $\xi_1 \parallel \xi_3$ when ξ_1 is not perpendicular to ξ_2.

This category indicates $\omega_3^T \hat{\omega}_1 = \mathbf{0}_{1 \times 3}$ and $\omega_1^T v_2 \neq 0$. Then θ_2 can be obtained by $\theta_2 = -z_1/\lambda_1$. θ_3 can be solved by substituting the value of θ_2 into Eq. (32) and the trigonometric relationship. θ_1 can be solved by combining the value of θ_2, the value of θ_3, and Eq. (4). If twists ξ_1 and ξ_3 intersect, the choices of points p_1 and p_3 should not be the point where the twists intersect.

Category 4: $\xi_1 \nparallel \xi_3$ when ξ_1 is not perpendicular to ξ_2. This category indicates $\omega_3^T \hat{\omega}_1 \neq \mathbf{0}_{1 \times 3}$ and $\omega_1^T v_2 \neq 0$. It is easy to know that the relationship between ξ_2 and ξ_3 in Eq. (6) is equivalent to the relationship between ξ_1 and ξ_2 in Eq. (1) for the RTR three-joint subproblem. Therefore, it is likely that ξ_2 is not perpendicular to ξ_3 in this category. If twists ξ_1 and ξ_3 intersect, the choices of points p_1 and p_3 should not be the point where the twists intersect. θ_2 is replaced with $\sin\theta_3$ and $\cos\theta_3$ in Eq. (31) and substituted into Eq. (32) as

$$\begin{aligned} & a_1 \sin^2\theta_3 + a_2 \cos^2\theta_3 + a_3 \sin\theta_3 \cos\theta_3 \\ & + a_4 \sin\theta_3 + a_5 \cos\theta_3 + a_6 = 0, \end{aligned} \tag{34}$$

where $a_1 = \lambda_2 x_1^2 - \lambda_1 x_1 x_3$, $a_2 = \lambda_2 y_1^2 - \lambda_1 y_1 y_3$, $a_3 = 2\lambda_2 x_1 y_1 - \lambda_1 x_3 y_1 - \lambda_1 x_1 y_3$, $a_4 = \lambda_1^2 x_2 + 2\lambda_2 x_1 z_1 - \lambda_1 \lambda_3 x_1 - \lambda_1 x_3 z_1$, $a_5 = \lambda_1^2 y_2 + 2\lambda_2 y_1 z_1 - \lambda_1 \lambda_3 y_1 - \lambda_1 y_3 z_1$, $a_6 = \lambda_2 z_1^2 - \lambda_1 \lambda_3 z_1 + \lambda_1^2 z_2$. Likewise, let $t = \tan\theta_3/2$. Then $\sin\theta_3 = 2t/(1+t^2)$ and $\cos\theta_3 = (1-t^2)/(1+t^2)$. Those are substituted into Eq. (34) as

$$m_1 t^4 + m_2 t^3 + m_3 t^2 + m_4 t + m_5 = 0, \tag{35}$$

where $m_1 = a_2 - a_5 + a_6$, $m_2 = 2(a_4 - a_3)$, $m_3 = 2(2a_1 - a_2 + a_6)$, $m_4 = 2(a_3 + a_4)$, $m_5 = a_2 + a_5 + a_6$. For the above quartic equation, the solution t is easily obtained by adopting Ferrari's method. The value of θ_3 can be solved as

$$\theta_3 = 2 \arctan t. \tag{36}$$

The value of θ_3 is substituted into Eq. (31) to solve θ_2. Similarly, θ_1 can be solved by combining the value of θ_2, the value of θ_3, and Eq. (4).

3.4 NAG method realization for the RTT subproblem

For the RTT three-joint subproblem, it is assumed that point p moves along ξ_3 by θ_3 to point c and point c moves along ξ_2 by θ_2 to point d, as shown in Fig. 9. This means that $c = p + \theta_3 v_3$ and $d = c + \theta_2 v_2$. It is obvious that points d and q are located on the circle C_1 normal to ξ_1. The twist ξ_1 passes through point p_1. This is easily accessible according to the geometric and algebraic constraints as

$$\omega_1^T (d - q) = 0, \tag{37}$$

$$\|q - p_1\| = \|d - p_1\|. \tag{38}$$

By substituting the expressions for points c and d into Eqs. (37) and (38), respectively, and squaring both sides of Eq. (38), the above two equations are transformed as follows:
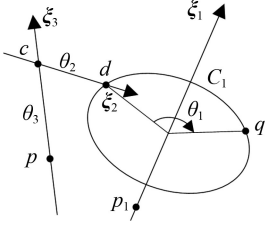
Fig. 9   General form of the RTT three-joint subproblem.

$$x_1\theta_2 + y_1\theta_3 + z_1 = 0, \tag{39}$$

$$x_2\theta_2{}^2 + y_2\theta_3{}^2 + a_1\theta_2\theta_3 + a_2\theta_2 + a_3\theta_3 + z_2 = 0, \tag{40}$$

where $x_1 = \boldsymbol{\omega}_1^{\mathrm{T}}\boldsymbol{v}_2$, $y_1 = \boldsymbol{\omega}_1^{\mathrm{T}}\boldsymbol{v}_3$, $z_1 = \boldsymbol{\omega}_1^{\mathrm{T}}(\boldsymbol{p}-\boldsymbol{q})$, $x_2 = y_2 = 1$, $a_1 = 2\boldsymbol{v}_3^{\mathrm{T}}\boldsymbol{v}_2$, $a_2 = 2(\boldsymbol{p}-\boldsymbol{p}_1)^{\mathrm{T}}\boldsymbol{v}_2$, $a_3 = 2(\boldsymbol{p}-\boldsymbol{p}_1)^{\mathrm{T}}\boldsymbol{v}_3$, and $z_2 = \|\boldsymbol{p}-\boldsymbol{p}_1\|^2 - \|\boldsymbol{q}-\boldsymbol{p}_1\|^2$.

For two arbitrary axes, $\boldsymbol{\omega}_1^{\mathrm{T}}\boldsymbol{\omega}_2 = 0$ holds if $\boldsymbol{\xi}_1$ is perpendicular to $\boldsymbol{\xi}_2$. The RTT three-joint subproblems for special configurations are explained and illustrated considering the characteristics of vertical joint axes.

Category 1: $\boldsymbol{\xi}_1$ is not perpendicular to $\boldsymbol{\xi}_3$ when $\boldsymbol{\xi}_1 \perp \boldsymbol{\xi}_2$.

This category indicates $\boldsymbol{\omega}_1^{\mathrm{T}}\boldsymbol{v}_3 \neq 0$ and $\boldsymbol{\omega}_1^{\mathrm{T}}\boldsymbol{v}_2 = 0$. θ_3 is easily obtained through $\theta_3 = -z_1/y_1$. The value of θ_3 is substituted into Eq. (40) to solve θ_2. The value of θ_1 can be solved by combining the value of θ_2, the value of θ_3, and Eq. (4).

Category 2: $\boldsymbol{\xi}_1$ is not perpendicular to $\boldsymbol{\xi}_2$ when $\boldsymbol{\xi}_1 \perp \boldsymbol{\xi}_3$.

This category indicates $\boldsymbol{\omega}_1^{\mathrm{T}}\boldsymbol{v}_2 \neq 0$ and $\boldsymbol{\omega}_1^{\mathrm{T}}\boldsymbol{v}_3 = 0$. θ_2 is easily obtained through $\theta_2 = -z_1/x_1$. The value of θ_2 is substituted into Eq. (40) to solve θ_3. The value of θ_1 can be solved by combining the value of θ_2, the value of θ_3, and Eq. (4).

Category 3: $\boldsymbol{\xi}_1$ is not perpendicular to $\boldsymbol{\xi}_2$ when $\boldsymbol{\xi}_1$ is not perpendicular to $\boldsymbol{\xi}_3$.

This category indicates $\boldsymbol{\omega}_1^{\mathrm{T}}\boldsymbol{v}_2 \neq 0$ and $\boldsymbol{\omega}_1^{\mathrm{T}}\boldsymbol{v}_3 \neq 0$. Combining Eqs. (39) and (40), θ_3 is used in place of θ_2 by $\theta_2 = -(y_1\theta_3 + z_1)/x_1$ as

$$m_1\theta_3^2 + m_2\theta_3 + m_3 = 0, \tag{41}$$

where $m_1 = x_2 y_1^2 + x_1^2 y_2 - a_1 x_1 y_1$, $m_2 = 2x_2 y_1 z_1 - a_1 x_1 z_1 - a_2 x_1 y_1 + a_3 x_1^2$, and $m_3 = x_2 z_1^2 - a_2 x_1 z_1 + x_1^2 z_2$. If $m_1 \neq 0$, then θ_3 can be solved by $\theta_3 = \left(-m_2 \pm \sqrt{m_2^2 - 4m_1 m_3}\right)/(2m_1)$; if $m_1 = 0$, then Eq. (41) is degraded to $m_2\theta_3 + m_3 = 0$. The value of θ_3 is substituted into Eq. (39) to solve θ_2. The value of θ_1 can be solved by combining the value of θ_2, the value of θ_3, and Eq. (4).

Category 4: $\boldsymbol{\xi}_1 \perp \boldsymbol{\xi}_2$ when $\boldsymbol{\xi}_1 \perp \boldsymbol{\xi}_3$.

This category indicates $\boldsymbol{\omega}_1^{\mathrm{T}}\boldsymbol{v}_2 = 0$ and $\boldsymbol{\omega}_1^{\mathrm{T}}\boldsymbol{v}_3 = 0$. Points c, d, p, and q are located on one plane, which is perpendicular to the twist $\boldsymbol{\xi}_1$. Therefore, the identity of Eq. (37) is always established. It is not possible to solve for the values of θ_2 and θ_3 by relying only on Eq. (40). The form of an infinite number of solutions is shown in Fig. 10. The arbitrary point on the red circle C_1 is the solution of the inverse kinematics.

3.5   NAG method realization for the TRT subproblem

For the TRT three-joint subproblem, it is assumed that point p moves along $\boldsymbol{\xi}_3$ by θ_3 to point c and point q moves along $\boldsymbol{\xi}_1$ by $-\theta_1$ to point d, as shown in Fig. 11. This means that $\boldsymbol{c} = \boldsymbol{p} + \theta_3\boldsymbol{v}_3$ and $\boldsymbol{d} = \boldsymbol{q} - \theta_1\boldsymbol{v}_1$. It is obvious that points c and d are located on the circle C_2 normal to $\boldsymbol{\xi}_2$. The twist $\boldsymbol{\xi}_2$ passes through point p_2. This is easily accessible according to the geometric and algebraic constraints as

$$\boldsymbol{\omega}_2^{\mathrm{T}}(\boldsymbol{c} - \boldsymbol{d}) = 0, \tag{42}$$

$$\|\boldsymbol{c} - \boldsymbol{p}_2\| = \|\boldsymbol{d} - \boldsymbol{p}_2\|. \tag{43}$$

By substituting the expressions for points c and d into Eqs. (42) and (43), respectively, and squaring both sides of Eq. (43), the above two equations are transformed as follows:

$$x_1\theta_1 + y_1\theta_3 + z_1 = 0, \tag{44}$$

$$x_2\theta_1{}^2 + y_2\theta_3{}^2 + a_1\theta_1 + a_2\theta_3 + z_2 = 0, \tag{45}$$

where $x_1 = \boldsymbol{\omega}_2^{\mathrm{T}}\boldsymbol{v}_1$, $y_1 = \boldsymbol{\omega}_2^{\mathrm{T}}\boldsymbol{v}_3$, $z_1 = \boldsymbol{\omega}_2^{\mathrm{T}}(\boldsymbol{p}-\boldsymbol{q})$, $x_2 = -1$, $y_2 = 1$, $a_1 = 2(\boldsymbol{q}-\boldsymbol{p}_2)^{\mathrm{T}}\boldsymbol{v}_1$, $a_2 = 2(\boldsymbol{p}-\boldsymbol{p}_2)^{\mathrm{T}}\boldsymbol{v}_3$, and $z_2 = \|\boldsymbol{p}-\boldsymbol{p}_2\|^2 - \|\boldsymbol{q}-\boldsymbol{p}_2\|^2$.

For two arbitrary axes, $\boldsymbol{\omega}_1^{\mathrm{T}}\boldsymbol{\omega}_2 = 0$ holds if $\boldsymbol{\xi}_1$ is perpendicular to $\boldsymbol{\xi}_2$. The TRT three-joint subproblems for special configurations are explained and illustrated considering the characteristics of vertical joint axes.

Category 1: $\boldsymbol{\xi}_2$ is not perpendicular to $\boldsymbol{\xi}_3$ when $\boldsymbol{\xi}_2 \perp \boldsymbol{\xi}_1$.

This category indicates $\boldsymbol{\omega}_2^{\mathrm{T}}\boldsymbol{v}_3 \neq 0$ and $\boldsymbol{\omega}_2^{\mathrm{T}}\boldsymbol{v}_1 = 0$. θ_3 is easily obtained through $\theta_3 = -z_1/y_1$. The value of θ_3 is substituted into Eq. (45) to solve θ_1. The value of θ_2 can be solved by combining the value of θ_1, the value of θ_3, and Eq. (4).

Category 2: $\boldsymbol{\xi}_2$ is not perpendicular to $\boldsymbol{\xi}_1$ when $\boldsymbol{\xi}_2 \perp \boldsymbol{\xi}_3$.

This category indicates $\boldsymbol{\omega}_2^{\mathrm{T}}\boldsymbol{v}_1 \neq 0$ and $\boldsymbol{\omega}_2^{\mathrm{T}}\boldsymbol{v}_3 = 0$. θ_1 is
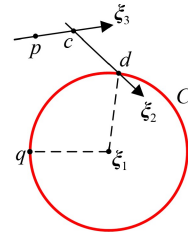
Fig. 10   Solution of RTT satisfying $\boldsymbol{\omega}_1 \perp \boldsymbol{v}_2$ and $\boldsymbol{\omega}_1 \perp \boldsymbol{v}_3$.
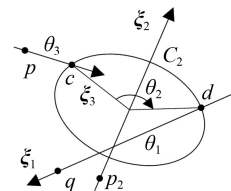

Fig. 11   General form of the TRT three-joint subproblem.

easily obtained through $\theta_1 = -z_1/x_1$. The value of θ_1 is substituted into Eq. (45) to solve θ_3. The value of θ_2 can be solved by combining the value of θ_1, the value of θ_3, and Eq. (4).

Category 3: $\boldsymbol{\xi}_2$ is not perpendicular to $\boldsymbol{\xi}_1$ when $\boldsymbol{\xi}_2$ is not perpendicular to $\boldsymbol{\xi}_3$.

This category indicates $\boldsymbol{\omega}_2^T \boldsymbol{v}_1 \neq 0$ and $\boldsymbol{\omega}_2^T \boldsymbol{v}_3 \neq 0$. Combining Eqs. (44) and (45), θ_3 is used in place of θ_1 by $\theta_1 = -(y_1\theta_3 + z_1)/x_1$ as

$$m_1\theta_3{}^2 + m_2\theta_3 + m_3 = 0, \tag{46}$$

where $m_1 = x_2 y_1^2 + x_1^2 y_2$, $m_2 = 2x_2 y_1 z_1 - a_1 x_1 y_1 + a_2 x_1^2$, and $m_3 = x_2 z_1^2 - a_1 x_1 z_1 + x_1^2 z_2$. If $m_1 \neq 0$, then θ_3 can be solved by $\theta_3 = \left(-m_2 \pm \sqrt{m_2^2 - 4m_1 m_3}\right)/(2m_1)$; on the contrary, if $m_1 = 0$, then Eq. (46) is degraded to $m_2\theta_3 + m_3 = 0$. The value of θ_3 is substituted into Eq. (44) to solve θ_1. The value of θ_2 can be solved by combining the value of θ_1, the value of θ_3, and Eq. (4).

Category 4: $\boldsymbol{\xi}_2 \perp \boldsymbol{\xi}_1$ when $\boldsymbol{\xi}_2 \perp \boldsymbol{\xi}_3$.

This category indicates $\boldsymbol{\omega}_2^T \boldsymbol{v}_1 = 0$ and $\boldsymbol{\omega}_2^T \boldsymbol{v}_3 = 0$. Points c, d, p, and q are located on one plane, which is perpendicular to the twist $\boldsymbol{\xi}_2$. Therefore, the identity of Eq. (42) is always established. It is not possible to identify the values of θ_1 and θ_3 by relying only on Eq. (45). The form of the infinite number of solutions is shown in Fig. 12. The arbitrary point on the red line segments is the inverse kinematics solution of θ_3.

3.6   NAG method realization for the TTT subproblem

For the TRT three-joint subproblem, it is assumed that point p moves along $\boldsymbol{\xi}_3$ by θ_3 to point c, point q moves along $\boldsymbol{\xi}_2$ by θ_2 to point d, and point d moves along $\boldsymbol{\xi}_1$ by θ_1 to point q, as shown in Fig. 13. Hence, it is easy to obtain the relationship equation between points p and q as

$$\boldsymbol{q} = \boldsymbol{p} + \theta_1 \boldsymbol{v}_1 + \theta_2 \boldsymbol{v}_2 + \theta_3 \boldsymbol{v}_3. \tag{47}$$

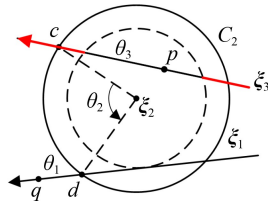Equation (47) can be converted into the matrix form as

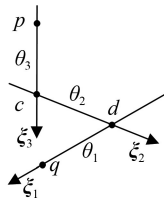Fig. 12   Solution of TRT satisfying $\omega_2 \perp v_1$ and $\omega_2 \perp v_3$.

Fig. 13   General form of the TTT three-joint subproblem.

$$V\boldsymbol{\theta} = \boldsymbol{Q}, \tag{48}$$

where $V = \begin{bmatrix} \boldsymbol{v}_1 & \boldsymbol{v}_2 & \boldsymbol{v}_3 \end{bmatrix}$, $\boldsymbol{\theta} = \begin{bmatrix} \theta_1 & \theta_2 & \theta_3 \end{bmatrix}^T$, $\boldsymbol{Q} = \boldsymbol{q} - \boldsymbol{p}$, and $\boldsymbol{Q}$ represents the difference between the vectors $\boldsymbol{q}$ and $\boldsymbol{p}$. The precondition for Eq. (48) to have a unique solution is that V is full-rank, that is, $\boldsymbol{\xi}_1$, $\boldsymbol{\xi}_2$, and $\boldsymbol{\xi}_3$ are linearly independent of one another. The solution of $\boldsymbol{\theta}$ is $\boldsymbol{\theta} = V^{-1}\boldsymbol{Q}$. If two axes are parallel, then V is not full-rank and there is an infinite number of solutions.

---

4   Results

To validate the effectiveness and practicability of the proposed NAG methods, the inverse kinematics simulations of arbitrary three-joint subproblems were implemented, and the simulation and master–slave tracking experiment based on the Huaque III minimally invasive surgical robot were carried out. Simulations were executed in MATLAB R2016b. According to the given joint motion ranges of each subproblem, 51 points were uniformly sampled to calculate the positions of the end-effector and then the NAG method was applied to calculate the joint angle values. The symbol x represents 51 integers from 1 to 51. In the simulation diagrams of joint inverse solutions, the symbol "o" represents the sample points of each joint while the symbol "+" represents the joint angles of the inverse solution. Note that the joint direction vectors need to be standardized before kinematic calculations can begin. There are several sets of joint angles of inverse solutions in simulations based on the NAG methods. The solutions that joint angles are in the angle ranges and the end posture is consistent with expected posture are screened. Then, the joint angles of inverse solutions are output and compared with sample points.

4.1   Simulations of arbitrary three-joint subproblems

4.1.1   Simulation of RRR subproblem

For the simulation of the RRR subproblem, category 4 is taken as an example to verify effectiveness of the NAG method. Three joints satisfy that $\boldsymbol{\xi}_2$ is neither parallel to $\boldsymbol{\xi}_1$ nor parallel to $\boldsymbol{\xi}_3$. In this case, the three joint axes do not intersect one another. The directions of the three joint axes are $\boldsymbol{\omega}_1 = [\,0 \ \ 0 \ \ 1\,]^T$, $\boldsymbol{\omega}_2 = [\,0 \ \ 1 \ \ 1\,]^T$, and $\boldsymbol{\omega}_3 = [\,2 \ \ 1 \ \ 0\,]^T$. The positions of the three reference points are $\boldsymbol{p}_1 = [\,1 \ \ 0 \ \ 0\,]^T$, $\boldsymbol{p}_2 = [\,5 \ \ 0 \ \ 0\,]^T$, and $\boldsymbol{p}_3 = [\,0 \ \ 5 \ \ 0\,]^T$. The position of initial point p is $\boldsymbol{p} = [\,5 \ \ -10 \ \ -10\,]^T$. The movement ranges of the three joints are determined as $\theta_1 = \dfrac{2\pi}{5}\cos\dfrac{x\pi}{25}$, $\theta_2 = \dfrac{\pi}{3}\cos\dfrac{x\pi}{25}$, and $\theta_3 = \dfrac{4\pi}{9}\cos\left(\dfrac{x\pi}{25} - \pi\right)$. The sample points and joint angles of the inverse solution are shown in Fig. 14. Clearly, the

joint angles of the inverse solution are coincident with the sample points.

4.1.2 Simulation of the RRT subproblem

For the simulation of the RRT subproblem, category 4 is taken as an example to verify the effectiveness of the NAG method. Three joints satisfy that $\boldsymbol{\xi}_2$ is neither parallel to $\boldsymbol{\xi}_1$ nor perpendicular to $\boldsymbol{\xi}_3$. The directions of the three joint axes are $\boldsymbol{\omega}_1 = [\,1 \quad 0 \quad 1\,]^{\mathrm{T}}$, $\boldsymbol{\omega}_2 = [\,0 \quad 1 \quad 1\,]^{\mathrm{T}}$, and $\boldsymbol{v}_3 = [\,2 \quad 1 \quad 0\,]^{\mathrm{T}}$. The positions of two reference points are $\boldsymbol{p}_1 = [\,0 \quad 0 \quad 0\,]^{\mathrm{T}}$ and $\boldsymbol{p}_2 = [\,5 \quad 0 \quad 0\,]^{\mathrm{T}}$. The position of the initial point p is $\boldsymbol{p} = [\,5 \quad -10 \quad -5\,]^{\mathrm{T}}$. The movement ranges of the three joints are determined as $\theta_1 = \dfrac{2\pi}{5}\cos\dfrac{x\pi}{25}$, $\theta_2 = \dfrac{\pi}{3}\cos\dfrac{x\pi}{25}$, and $\theta_3 = 50\cos\left(\dfrac{x\pi}{25}-\pi\right)$. The sample points and joint angles of the inverse solution are shown in Fig. 15. It is easy to know that the sample

points and the joint angles of the inverse solution are coincident.

4.1.3 Simulation of the RTR subproblem

For the simulation of the RTR subproblem, category 4 is taken as an example to verify the effectiveness of the NAG method. Three joints satisfy that $\boldsymbol{\xi}_2$ is neither parallel to $\boldsymbol{\xi}_1$ nor perpendicular to $\boldsymbol{\xi}_3$. The directions of three joint axes are $\boldsymbol{\omega}_1 = [\,1 \quad 0 \quad 1\,]^{\mathrm{T}}$, $\boldsymbol{v}_2 = [\,0 \quad 1 \quad 1\,]^{\mathrm{T}}$, and $\boldsymbol{\omega}_3 = [\,2 \quad 1 \quad 0\,]^{\mathrm{T}}$. The positions of two reference points are $\boldsymbol{p}_1 = [\,0 \quad 0 \quad 0\,]^{\mathrm{T}}$ and $\boldsymbol{p}_3 = [\,0 \quad 5 \quad 0\,]^{\mathrm{T}}$. The position of initial point p is $\boldsymbol{p} = [\,5 \quad -10 \quad -5\,]^{\mathrm{T}}$. The movement ranges of the three joints are determined as $\theta_1 = \dfrac{2\pi}{5}\cos\dfrac{x\pi}{25}$, $\theta_2 = 50\cos\left(\dfrac{x\pi}{25}-\pi\right)$, and $\theta_3 = \dfrac{\pi}{3}\cos\dfrac{x\pi}{25}$. The sample points and joint angles of the inverse solution are shown in Fig. 16. Clearly, the sample points and joint angles of the inverse solution are coincident.
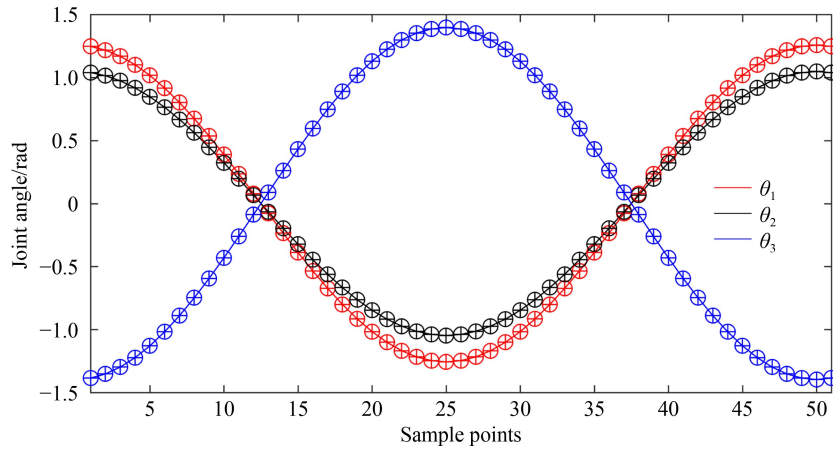

Fig. 14   Sample points and joint angles of the inverse solution of RRR subproblem.
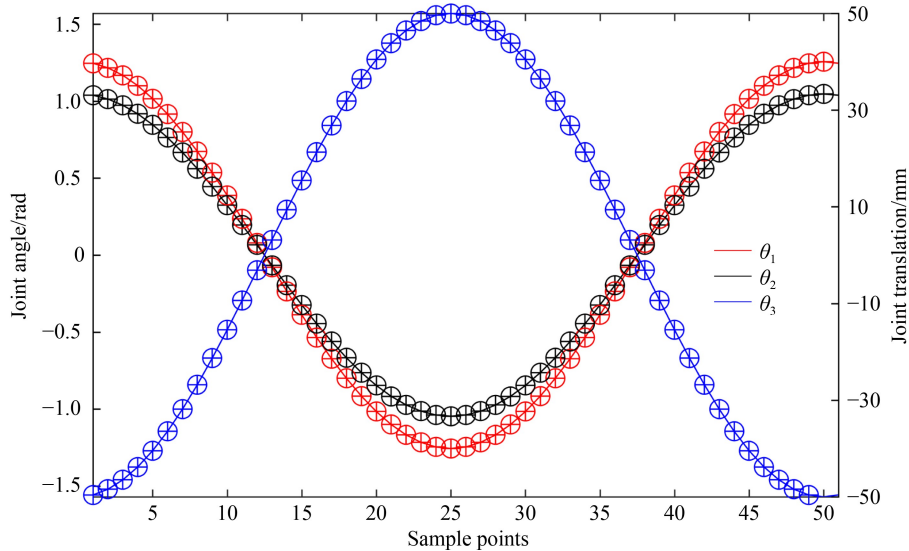

Fig. 15   Sample points and joint angles of the inverse solution of RRT subproblem.

4.1.4 Simulation of the RTT subproblem

For the simulation of the RTT subproblem, category 3 is taken as an example to verify the effectiveness of the NAG method. Three joints satisfy that $\boldsymbol{\xi}_2$ is neither parallel to $\boldsymbol{\xi}_1$ nor perpendicular to $\boldsymbol{\xi}_3$. The directions of the three joint axes are $\boldsymbol{\omega}_1 = [\,1 \quad 0 \quad 1\,]^{\mathrm{T}}$, $\boldsymbol{v}_2 = [\,0 \quad 1 \quad 1\,]^{\mathrm{T}}$, and $\boldsymbol{v}_3 = [\,2 \quad 1 \quad 0\,]^{\mathrm{T}}$. The position of reference points is $\boldsymbol{p}_1 = [\,0 \quad 0 \quad 0\,]^{\mathrm{T}}$. The position of the initial point p is $\boldsymbol{p} = [\,5 \quad -10 \quad -5\,]^{\mathrm{T}}$. The movement ranges of the three joints are determined as $\theta_1 = \dfrac{2\pi}{5}\cos\dfrac{x\pi}{25}$, $\theta_2 = 50\cos\left(\dfrac{x\pi}{25} - \pi\right)$, and $\theta_3 = 50\cos\dfrac{x\pi}{25}$. The sample points and joint angles of the inverse solution are shown in Fig. 17. Apparently, the joint angles of the inverse solution are coincident with the sample points.

4.1.5 Simulation of the TRT subproblem

For the simulation of the TRT subproblem, category 3 is taken as an example to verify the effectiveness of the NAG method. Three joints satisfy that $\boldsymbol{\xi}_2$ is not perpendicular to $\boldsymbol{\xi}_1$ when $\boldsymbol{\xi}_2$ is not perpendicular to $\boldsymbol{\xi}_3$. The directions of three joint axes are $\boldsymbol{v}_1 = [\,1 \quad 0 \quad 1\,]^{\mathrm{T}}$, $\boldsymbol{\omega}_2 = [\,0 \quad 1 \quad 1\,]^{\mathrm{T}}$, and $\boldsymbol{v}_3 = [\,2 \quad 1 \quad 0\,]^{\mathrm{T}}$. The position of reference points is $\boldsymbol{p}_2 = [\,5 \quad 0 \quad 0\,]^{\mathrm{T}}$. The position of initial point p is $\boldsymbol{p} = [\,5 \quad -10 \quad -5\,]^{\mathrm{T}}$. The movement ranges of the three joints are determined as $\theta_1 = 50\cos\left(\dfrac{x\pi}{25} - \pi\right)$, $\theta_2 = \dfrac{2\pi}{5}\cos\dfrac{x\pi}{25}$, and $\theta_3 = 50\cos\dfrac{x\pi}{25}$. The sample points and joint angles of the inverse solution are shown in Fig. 18. Obviously, the joint angles of the inverse solution and the sample points remain coincident.
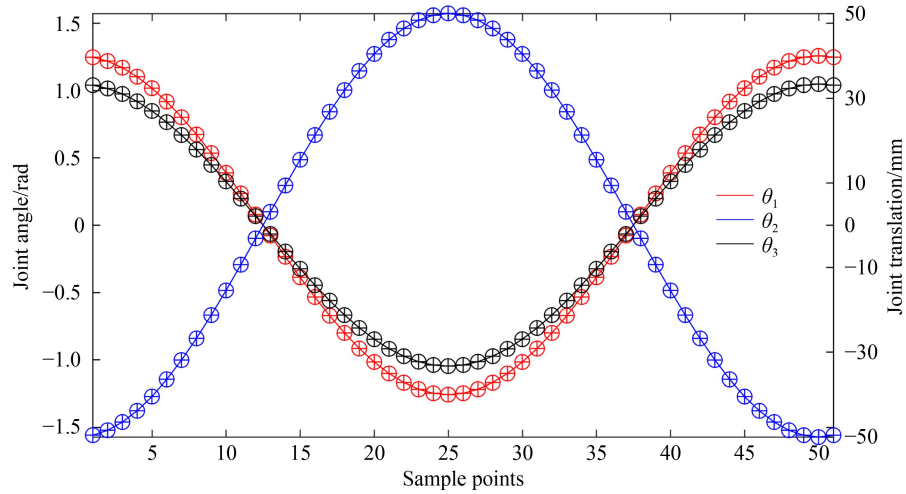

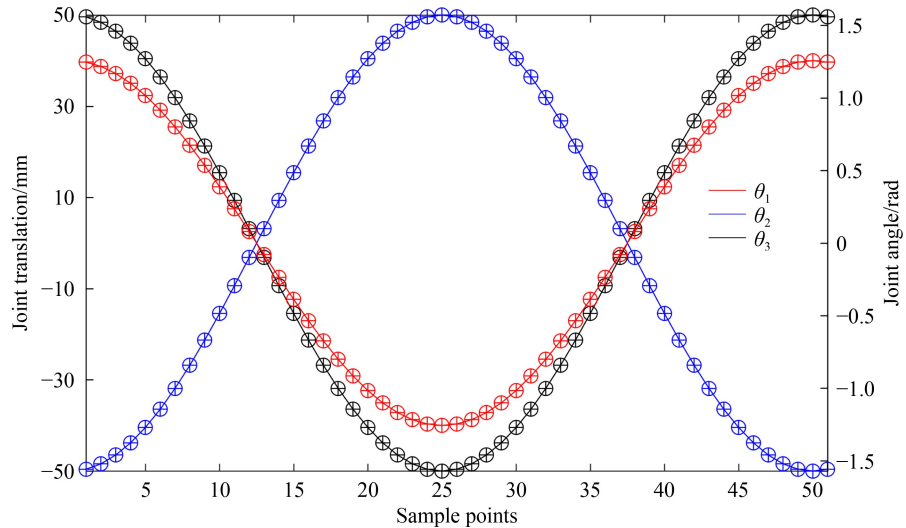**Fig. 16** Sample points and joint angles of the inverse solution of RTR subproblem.

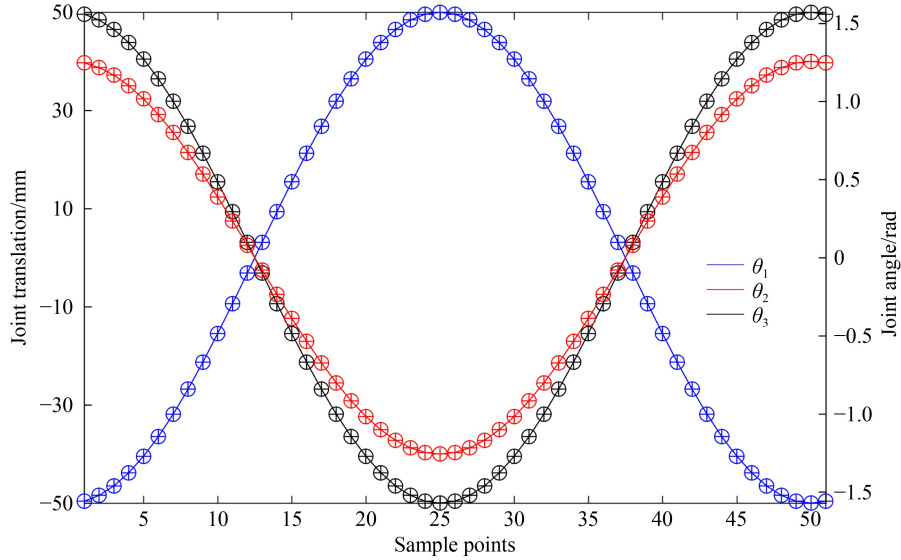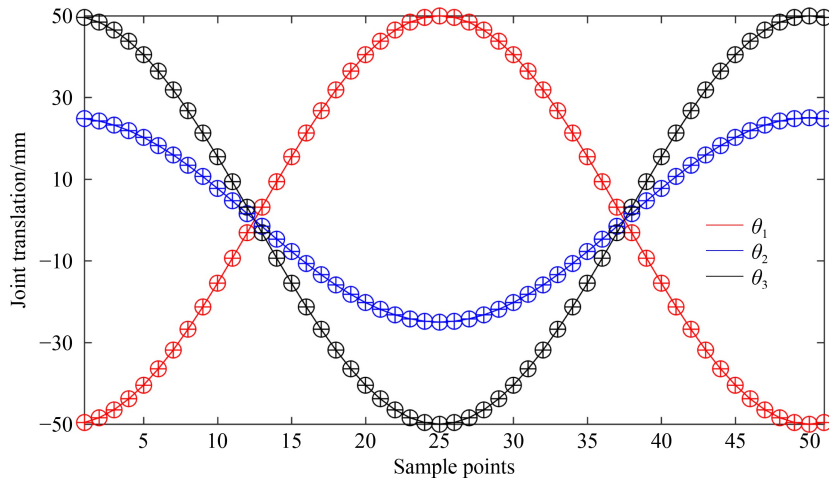**Fig. 17** Sample points and joint angles of the inverse solution of RTT subproblem.

4.1.6   Simulation of the TTT subproblem

For the simulation of the TTT subproblem, three joints are linearly independent of one another. The directions of the three joint axes are $\boldsymbol{v}_1 = [\,1 \quad 0 \quad 1\,]^T$, $\boldsymbol{v}_2 = [\,0 \quad 1 \quad 1\,]^T$, and $\boldsymbol{v}_3 = [\,2 \quad 1 \quad 0\,]^T$. The position of the initial point p is $\boldsymbol{p} = [\,5 \quad -10 \quad -5\,]^T$. The movement ranges of the three joints are determined as $\theta_1 = 50\cos\left(\dfrac{x\pi}{25} - \pi\right)$, $\theta_2 = 25\cos\dfrac{x\pi}{25}$, and $\theta_3 = 50\cos\dfrac{x\pi}{25}$. The sample points and joint angles of the inverse solution are shown in Fig. 19. Distinctly, the joint angles of the inverse solution are coincident with the sample points.

4.2   Simulation of 6-DOF problem based on Huaque III surgical robot

Huaque III minimally invasive surgical robot [30]

includes two instrument manipulators and one endoscopy manipulator. The instrument manipulator consists of passive joints, active joints, and a surgical instrument, as shown in Fig. 20. Passive joints are used to locate the remote center of motion (RCM) at any point in space. Active joints are used to achieve rotation and translational motion around the RCM point. Surgical instrument coordinates with active joints to adjust the position and posture of the end-effector. Note that three joint axes of instrument do not intersect at one point, that is, it does not satisfy the Pieper criterion. Joints 7 and 8 are coaxial, and joints 7 and 8 are prismatic and rotary joints, respectively. Two joints can be exchanged on the premise that the order of interchanging joints does not affect the end-effector pose [31]. To conveniently solve the inverse solution, joints 7 and 8 are swapped in turn. The screw representation and reference coordinate points of each joint axis are as follows:

Fig. 18   Sample points and joint angles of the inverse solution of TRT subproblem.

Fig. 19   Sample points and joint angles of the inverse solution of TTT subproblem.
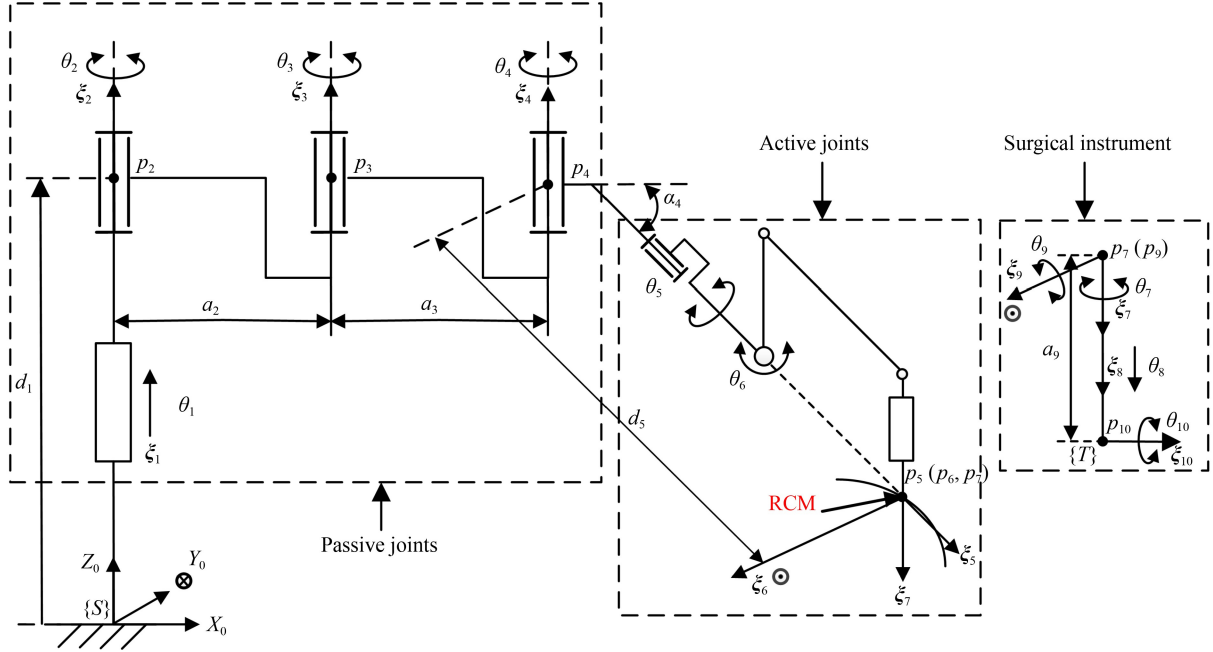
Fig. 20 Structure diagram of the instrument manipulator of Huaque III surgical robot.

$$\boldsymbol{\omega}_1 = \boldsymbol{\omega}_8 = \begin{bmatrix} 0 \\ 0 \\ 0 \end{bmatrix}, \boldsymbol{\omega}_2 = \boldsymbol{\omega}_3 = \boldsymbol{\omega}_4 = \begin{bmatrix} 0 \\ 0 \\ 1 \end{bmatrix}, \boldsymbol{\omega}_5 = \begin{bmatrix} \cos\alpha_4 \\ 0 \\ -\sin\alpha_4 \end{bmatrix},$$

$$\boldsymbol{\omega}_6 = \boldsymbol{\omega}_9 = \begin{bmatrix} 0 \\ -1 \\ 0 \end{bmatrix}, \boldsymbol{\omega}_7 = \begin{bmatrix} 0 \\ 0 \\ -1 \end{bmatrix}, \boldsymbol{\omega}_{10} = \begin{bmatrix} 1 \\ 0 \\ 0 \end{bmatrix},$$

$$\tag{49}$$

$$\boldsymbol{r}_2 = \begin{bmatrix} 0 \\ 0 \\ d_1 \end{bmatrix}, \boldsymbol{r}_3 = \begin{bmatrix} a_2 \\ 0 \\ d_1 \end{bmatrix}, \boldsymbol{r}_4 = \begin{bmatrix} a_2 + a_3 \\ 0 \\ d_1 \end{bmatrix},$$

$$\boldsymbol{r}_5 = \boldsymbol{r}_6 = \boldsymbol{r}_7 = \boldsymbol{r}_9 = \begin{bmatrix} a_2 + a_3 + d_5\cos\alpha_4 \\ 0 \\ d_1 - d_5\sin\alpha_4 \end{bmatrix},$$

$$\boldsymbol{r}_{10} = \begin{bmatrix} a_2 + a_3 + d_5\cos\alpha_4 \\ 0 \\ d_1 - d_5\sin\alpha_4 - a_9 \end{bmatrix}. \tag{50}$$

The forward kinematics solution of the Huaque III surgical instrument end-effector is

$$\boldsymbol{g}_{st}(\boldsymbol{\theta}) = \prod_{i=1}^{10} e^{\hat{\boldsymbol{\xi}}_i\theta_i} \boldsymbol{g}_{st}(\boldsymbol{0}), \tag{51}$$

where $\boldsymbol{g}_{st}(\boldsymbol{0})$ and $\boldsymbol{g}_{st}(\boldsymbol{\theta})$ respectively represent the initial transformation matrix and transformation matrix at different joint angles of the tool frame. The passive joint remains stationary during the operation, and Eq. (51) can be transformed as

$$\left(\prod_{i=1}^{4} e^{\hat{\boldsymbol{\xi}}_i\theta_i}\right)^{-1} \boldsymbol{g}_{st}(\boldsymbol{\theta}) \boldsymbol{g}_{st}^{-1}(\boldsymbol{0}) = \prod_{i=5}^{10} e^{\hat{\boldsymbol{\xi}}_i\theta_i}. \tag{52}$$

Let $\boldsymbol{g}_1 = \left(\prod_{i=1}^{4} e^{\hat{\boldsymbol{\xi}}_i\theta_i}\right)^{-1} \boldsymbol{g}_{st}(\boldsymbol{\theta}) \boldsymbol{g}_{st}^{-1}(\boldsymbol{0})$. Thus, the above formula is converted as

$$\boldsymbol{g}_1\left(\prod_{i=8}^{10} e^{\hat{\boldsymbol{\xi}}_i\theta_i}\right)^{-1} = \prod_{i=5}^{7} e^{\hat{\boldsymbol{\xi}}_i\theta_i}. \tag{53}$$

Joints 5, 6, and 7 are all rotary joints, and their axes converge at a point. The homogeneous coordinate vector of the intersection point is multiplied on both sides of the above equation by right, and according to the position preservation principle, the equation can be obtained as

$$\left(\prod_{i=8}^{10} e^{\hat{\boldsymbol{\xi}}_i\theta_i}\right) \boldsymbol{g}_1^{-1} \tilde{\boldsymbol{p}}_5 = \tilde{\boldsymbol{p}}_5, \tag{54}$$

where $\tilde{\boldsymbol{p}}_5 = [\,\boldsymbol{r}_5^{\mathrm{T}} \quad 1\,]^{\mathrm{T}}$. $\boldsymbol{r}_5$ and $\tilde{\boldsymbol{p}}_5$ represent the position vector and homogeneous coordinate of the point p_5. Let $\tilde{\boldsymbol{q}}_1 = \boldsymbol{g}_1^{-1}\tilde{\boldsymbol{p}}_5$, then θ_8, θ_9, and θ_{10} can be solved by the NAG method for the RRT subproblem. Next, θ_5, θ_6, and θ_7 can be solved by the NAG method for the RRR subproblem by substituting the joint angles of θ_8, θ_9, and θ_{10} into Eq. (53). The parameter values of the minimally invasive surgical robot are $d_1 = 1000$ mm, $a_2 = 500$ mm, $a_3 = 500$ mm, $\alpha_4 = \pi/4$, $d_5 = 800$ mm, and $a_9 = 10$ mm. The angles of the passive joints are constant as $\theta_1 = 200$, $\theta_2 = \pi/9$, $\theta_3 = -\pi/18$, and $\theta_4 = -\pi/18$. The motion ranges of the joints are $\theta_5 \in [-\pi/, 2, \pi/2]$, $\theta_6 \in [-\pi/3, \pi/3]$, $\theta_7 \in [-\pi, \pi]$, $\theta_8 \in [100, 350]$ mm, $\theta_9 \in (-\pi/2, \pi/2)$, and $\theta_{10} \in (-\pi/2, \pi/2)$. The motion curves of the other joints are $\theta_5 = \dfrac{\pi}{2}\sin\dfrac{x\pi}{25}$, $\theta_6 = \dfrac{\pi}{3}\sin\dfrac{(x-25)\pi}{25}$, $\theta_7 = \dfrac{2\pi}{9}$ $\cdot\sin\dfrac{(x-25)\pi}{25}$, $\theta_8 = 4(x-1) + 100$, $\theta_9 = \dfrac{4\pi}{9}\sin\dfrac{x\pi}{25}$, and

$\theta_{10} = \dfrac{2\pi}{9}\sin\dfrac{x\pi}{25}$. The sample points and joint angles of the inverse solution are shown in Fig. 21. It is evident that the joint angles of the inverse solution are coincident with the sample points.

4.3 Master–slave tracking experiment based on the Huaque III surgical robot

The surgeon operates the master manipulator on the master console to control the slave manipulator and perform a series of surgical operations (Fig. 22). The two-stage approximation and compensation method [5] has relatively higher accuracy and faster compensation speed, and thus the compensation method is chosen as a contrast to the closed-form solution for the Huaque III surgical robot. The master manipulator is moved in a random

curve trajectory, and the movement trajectory from the slave manipulator is recorded based on two methods. The trajectories of the master and instrument manipulators are compared in the situation where the master manipulator trajectories have been reduced to one-fourth and their tracking errors are calculated, as shown in Figs. 23 and 24. In Figs. 23(a) and 23(b), the incremental ranges of the slave manipulator trajectory are $x \in (-15, 15)$ mm, $y \in (-10, 30)$ mm, and $z \in (-10, 20)$ mm for the closed-form solution, while the incremental ranges of the slave manipulator trajectory are $x \in (-20, 30)$ mm, $y \in (-15, 5)$ mm, and $z \in (-15, 20)$ mm for the compensation method. The motion ranges of the two methods are close. Additionally, the trajectories of the slave manipulator are very close to those of the master manipulator. The end-effector tracking errors of master and slave manipulators
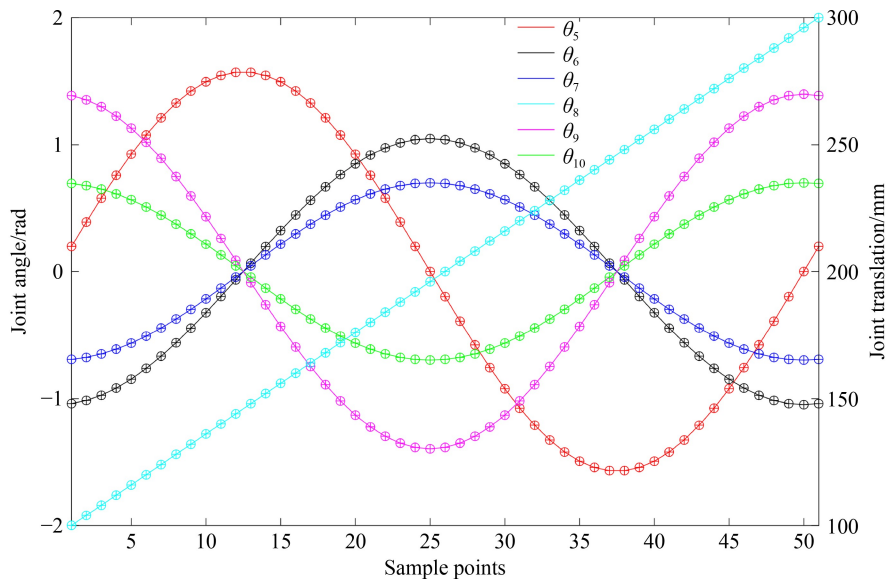

Fig. 21 Sample points and joint angles of the inverse solution for Huaque III surgical robot.
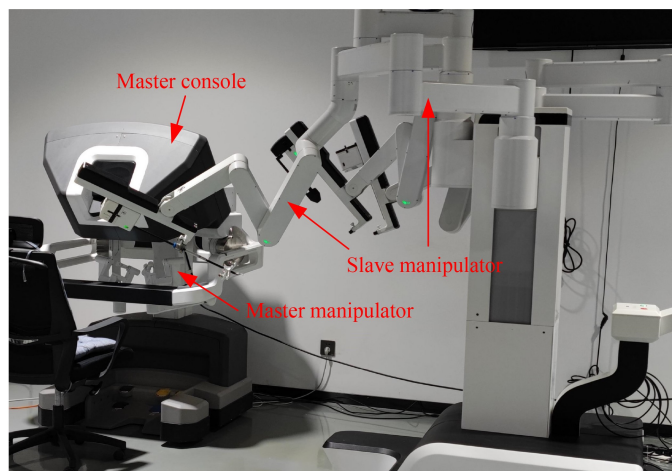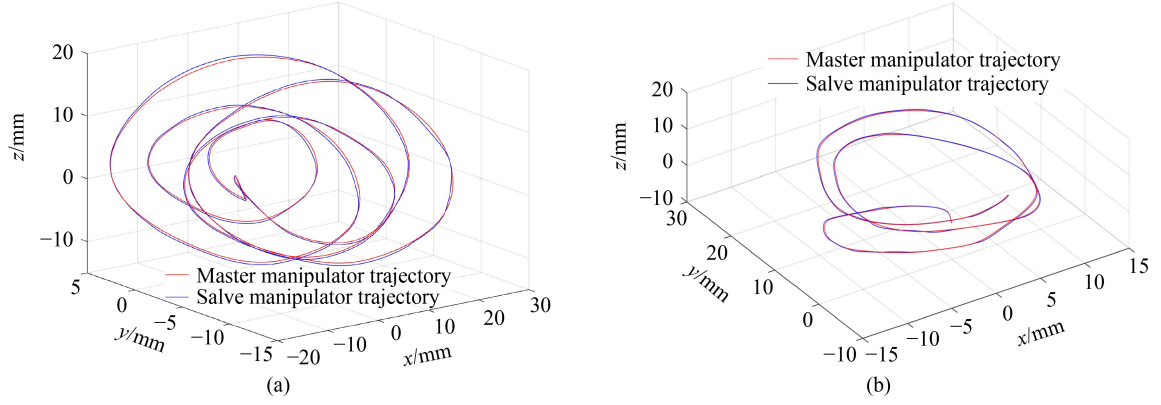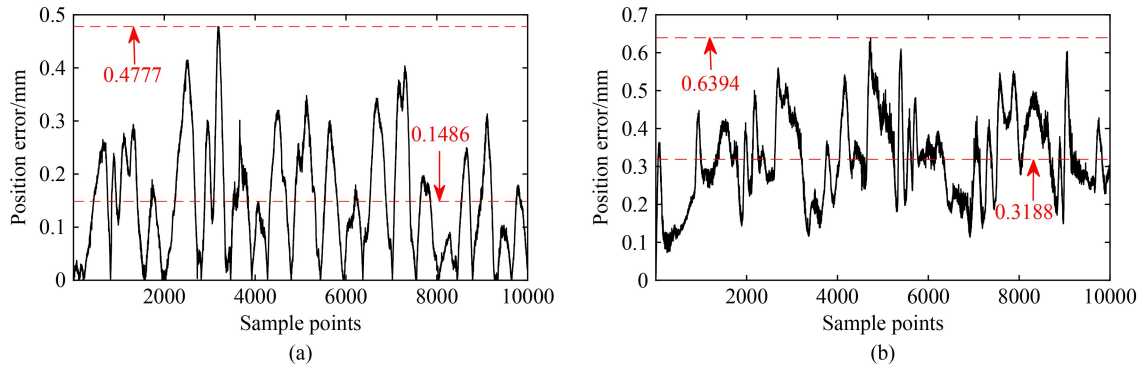

Fig. 22 Huaque III minimally invasive surgical robot.

Fig. 23   Movement trajectories for two methods: (a) closed-form solution and (b) compensation solution.

Fig. 24   End-effector tracking errors for two methods: (a) closed-form solution and (b) compensation solution.

are very small. The mean and maximum errors of the master–slave tracking experiment are 0.1486 and 0.4777 mm, respectively, for the closed-form solution, while the mean and maximum errors are 0.3188 and 0.6394 mm, respectively, for the compensation method. The mean and maximum tracking errors of the closed-form solution are 53.59% and 25.29% less than that of the compensation method. The maximum tracking errors are less than the absolute positioning accuracy of the robot at 1.4 mm, which meets the control accuracy requirements of the master–slave tracking of the surgical robot.

5   Conclusions

In this paper, the NAG methods are presented, and on their basis, the general closed-form inverse kinematics for all types of three-joint subproblems are obtained. The preconditions consisting of the geometric and algebraic constraints are applied to solve the inverse kinematics of three-joint subproblems. Special postures (parallel, perpendicular, and intersect) of three-joint subproblems are also discussed and illustrated. The inverse kinematics of arbitrary three-joint subproblems in an arbitrary postural relationship can be solved by the NAG methods. The inverse kinematics simulations of all three-joint

subproblems are implemented, and the inverse solutions are consistent with the given joint angles. Simulation results validate the general closed-form inverse kinematics. The simulation and master–slave tracking experiment are carried out to verify the NAG methods of the RRR and RRT subproblems based on the experimental platform of the Huaque III minimally invasive surgical robot. The simulation result shows that the inverse solutions are consistent with six sets given joint angles. The mean and maximum of the master–slave tracking experiment for the closed-form solution are 0.1486 and 0.4777 mm, respectively, while the mean and maximum of the master–slave tracking experiment for the compensation method are 0.3188 and 0.6394 mm, respectively. The mean and maximum tracking errors of the closed-form solution are 53.59% and 25.29% less than those of the compensation method. Clearly, the closed-form solution is superior to the compensation method. The general closed-form inverse kinematics are validated according to the simulation and experiment results. The arbitrary three-joint subproblems expand the Paden–Kahan subproblems, and the proposed general closed-form inverse kinematics can be combined and widely applied in series, parallel, reconfigurable, and other types of robots.

Nomenclature

Abbreviations

D–H	Denavit–Harbenterg
DOF	Degree-of-freedom
NAG	Novel algebraic geometric
POE	Product of exponential
R, T	revolute joint and translational joint, respectively
RCM	Remote center of motion

Variables

c, d, p, p_1, p_2, p_3, and q	Position vectors of points c, d, p, p_1, p_2, p_3, and q, respectively
$g_{st}(0)$, $g_{st}(\theta)$	Initial transformation matrix and transformation matrix at different joint angles of the tool frame, respectively
l_{c2}	Distance between points c and p_2
l_{ij} $(i, j = 1, 2, 3)$	Distance between points p_i and p_j
m	Difference between the vectors p_3 and p
$\tilde{p}_5$	Homogeneous coordinate of point p_5
$\tilde{q}$, $\tilde{p}$	Homogeneous coordinate of points q and p, respectively
r	Position vector of the reference point r of the revolute joint axis
r_5	Position vector of point p_5
v	Unit directional vector of the translational joint axis
θ_i	Generalized angle of the ith joint
δ	Distance between two vectors s and t, $\delta = \|s - t\|$
ω	Unit directional vector of the revolute joint axis
$\hat{\omega}$	Skew-symmetric matrices of ω
ξ	Joint twist
ξ_i $(i = 1, 2, 3)$	Twist coordinate of the ith joint axis
$\hat{\xi}_i$ $(i = 1, 2, 3)$	Instantaneous joint twist of the ith joint axis

References

1. Husty M L, Pfurner M, Schröcker H P. A new and efficient algorithm for the inverse kinematics of a general serial 6R manipulator. Mechanism and Machine Theory, 2007, 42(1): 66–81

2. Murray R M, Li Z X, Sastry S S. A Mathematical Introduction to Robotic Manipulation. Boca Raton: CRC Press, 1994

3. Niu G J, Pan B, Ai Y, Fu Y L. Intuitive control algorithm of a novel minimally invasive surgical robot. Computer Assisted Surgery, 2016, 21(sup1): 92–101

4. Stoica A, Pisla D, Andras S, Gherman B, Gyurka B Z, Plitea N. Kinematic, workspace and singularity analysis of a new parallel robot used in minimally invasive surgery. Frontiers of Mechanical Engineering, 2013, 8(1): 70–79

5. Tang A L. Research on the teleoperation motion control strategy for a master-slave minimally invasive surgical robot. Dissertation for the Doctoral Degree. Shanghai: Shanghai Jiao Tong University, 2014 (in Chinese)

6. Zhang F, Teng S, Wang Y F, Guo Z J, Wang J J, Xu R L. Design of bionic goat quadruped robot mechanism and walking gait planning. International Journal of Agricultural and Biological Engineering, 2020, 13(5): 32–39

7. Lakhal O, Melingui A, Merzouki R. Hybrid approach for modeling and solving of kinematics of a compact bionic handling assistant manipulator. IEEE/ASME Transactions on Mechatronics, 2016, 21(3): 1326–1335

8. Yang H, Fang H R, Fang Y F, Li X Y. Dimensional synthesis of a novel 5-DOF reconfigurable hybrid perfusion manipulator for large-scale spherical honeycomb perfusion. Frontiers of Mechanical Engineering, 2021, 16(1): 46–60

9. Zhang W X, Lu S N, Ding X L. Recent development on innovation design of reconfigurable mechanisms in China. Frontiers of Mechanical Engineering, 2019, 14(1): 15–20

10. Kim J, Jie W, Kim H, Lee M C. Modified configuration control with potential field for inverse kinematics solution of redundant manipulator. IEEE/ASME Transactions on Mechatronics, 2021, 26(4): 1782–1790

11. Patil A, Kulkarni M, Aswale A. Analysis of the inverse kinematics for 5 DOF robot arm using D–H parameters. In: Proceedings of 2017 IEEE International Conference on Real-time Computing and Robotics (RCAR). Okinawa: IEEE, 2017, 688–693

12. Xu J, Song K C, He Y, Dong Z P, Yan Y H. Inverse kinematics for 6-DOF serial manipulators with offset or reduced wrists via a hierarchical iterative algorithm. IEEE Access: Practical Innovations, Open Solutions, 2018, 6: 52899–52910

13. Soleimani Amiri M, Ramli R. Intelligent trajectory tracking behavior of a multi-joint robotic arm via genetic–swarm optimization for the inverse kinematic solution. Sensors, 2021, 21(9): 3171

14. Zhou H B, Zhou S, Yu J, Zhang Z D, Liu Z Z. Trajectory optimization of pickup manipulator in obstacle environment based on improved artificial potential field method. Applied sciences, 2020, 10(3): 935

15. Tian X M, Xu Y. Low delay control algorithm of robot arm for minimally invasive medical surgery. IEEE Access: Practical Innovations, Open Solutions, 2020, 8: 93548–93560

16. Xu Z H, Li S, Zhou X F, Yan W, Cheng T B, Huang D. Dynamic neural networks based kinematic control for redundant manipulators with model uncertainties. Neurocomputing, 2019, 329: 255–266

17. Gallardo-Alvarado J, Aguilar-Nájera C R, Casique-Rosas L, Rico-

Martínez J M, Islam M N. Kinematics and dynamics of 2(3-RPS) manipulators by means of screw theory and the principle of virtual work. Mechanism and Machine Theory, 2008, 43(10): 1281–1294

18. Hayati S A. Robot arm geometric link parameter estimation. In: Proceedings of the 22nd IEEE Conference on Decision & Control. San Antonio: IEEE, 1983, 1477–1483

19. Zhao R B, Shi Z P, Guan Y, Shao Z Z, Zhang Q Y, Wang G H. Inverse kinematic solution of 6R robot manipulators based on screw theory and the Paden–Kahan subproblem. International Journal of Advanced Robotic Systems, 2018, 15(6): 1729881418818297

20. Paden B E. Kinematics and control of robot manipulators. Dissertation for the Doctoral Degree. Berkeley: University of California, 1985

21. Chen I M, Gao Y. Closed-form inverse kinematics solver for reconfigurable robots. In: Proceedings of 2001 ICRA. IEEE International Conference on Robotics and Automation (Cat. No.01CH37164). Seoul: IEEE, 2001, 3: 2395–2400

22. Zhao J, Wang W D, Gao Y S, Cai H G. Generation of closed-form inverse kinematics for reconfigurable robots. Frontiers of Mechanical Engineering in China, 2008, 3(1): 91–96

23. Tan Y S, Cheng P L, Xiao A P. Solution for a new sub-problem in screw theory and its' application in the inverse kinematics of a manipulator. Applied Mechanics and Materials, 2010, 34–35: 271–275

24. Leoro J, Hsiao T S, Betancourt C. A new geometric subproblem to extend solvability of inverse kinematics based on screw theory for 6R robot manipulators. International Journal of Control, Automation, and Systems, 2021, 19(1): 562–573

25. Chen Q C, Zhu S Q, Zhang X Q. Improved inverse kinematics algorithm using screw theory for a six-DOF robot manipulator. International Journal of Advanced Robotic Systems, 2015, 12(10): 140

26. Li W W, Zhou G B, Zhou X F, Chen Z L, Wu L, Zeng S F. Kinematics analysis of generalized SRU manipulator based on screw theory. In: Proceedings of 2018 the 3rd International Conference on Robotics and Automation Engineering (ICRAE). Guangzhou: IEEE, 2018, 160–165

27. Wang H X, Lu X, Zhang Z Y, Li Y X, Sheng C Y, Gao L. A novel second subproblem for two arbitrary axes of robots. International Journal of Advanced Robotic Systems, 2018, 15(2): 1729881418769194

28. Wang H X, Lu X, Sheng C Y, Zhang Z G, Cui W, Li Y X. General frame for arbitrary 3R subproblems based on the POE model. Robotics and Autonomous Systems, 2018, 105: 138–145

29. Wang Y C, Ding X L, Tang Z X, Hu C W, Xu K. A novel analytical inverse kinematics method for SSRMS-type space manipulators based on the POE formula and the Paden-Kahan subproblem. International Journal of Aerospace Engineering, 2021, 6690696

30. Song T, Pan B, Niu G J, Fu Y L. Preoperative planning algorithm for robot-assisted minimally invasive cholecystectomy combined with appendectomy. IEEE Access: Practical Innovations, Open Solutions, 2020, 8: 177100–177111

31. Yu L T, Wang W J, Wang Z Y, Gu Q, Wang L. Acquisition method of inverse kinematics analytical solutions for a class of robots dissatisfying the Pieper criterion. Robot, 2016, 38(4): 486–494 (in Chinese)